

Article

Paleoproterozoic Metamorphism of the Archean Tuntsa Suite, Northern Fennoscandian Shield

Pentti Hölttä ^{1,*}, Tiia Kivisaari ^{2,†}, Hannu Huhma ¹, Gavyn Rollinson ³, Matti Kurhila ¹ and Alan R. Butcher ¹

¹ Geological Survey of Finland, P.O. Box 96, FI-02151 Espoo, Finland; hannu.huhma@gmail.com (H.H.); matti.kurhila@gtk.fi (M.K.); alan.butcher@gtk.fi (A.R.B.)

² Department of Geosciences & Geography, University of Helsinki, 00100 Helsinki, Finland; tiia.kivisaari@gmail.com

³ Camborne School of Mines, College of Engineering, Mathematics and Physical Sciences, University of Exeter, Penryn TR10 9FE, UK; g.k.rollinson@exeter.ac.uk

* Correspondence: pentti.holtta@gtk.fi

† Present address: Anglo American, FI-99600 Sodankylä, Finland.

Received: 21 October 2020; Accepted: 14 November 2020; Published: 19 November 2020



Abstract: The Tuntsa Suite is a polymetamorphic Archean complex mainly consisting of metasedimentary gneisses. At least two strong metamorphic events can be distinguished in the area. The first took place at high temperatures in the Neoproterozoic at around 2.70–2.64 Ga, indicated by migmatization and U-Pb ages of metamorphic zircon. During the Paleoproterozoic, metasedimentary gneisses were penetratively deformed and recrystallized under medium pressures producing staurolite, kyanite and garnet-bearing mineral assemblages. The suggested Paleoproterozoic PT path was clockwise where the temperature and pressure first increased to 540–550 °C and 6 kbar, crystallizing high Ca/low Mg garnet cores. The mineral compositions show that commonly garnet core was not in chemical equilibrium with staurolite but crystallized earlier, although garnet-staurolite-kyanite assemblages are common. The temperature and pressure increased to c. 650 °C and 8 kbars where staurolite and kyanite coexist. This was followed by decompression down to c. 550–600 °C and 3–4 kbars, shown by andalusite crystallization and cordierite formed in the breakdown of staurolite and biotite + kyanite. The observed garnet zoning where Mg increases and Ca decreases from the core to the rim was developed with both increasing and decreasing pressure, depending on the effective bulk composition. The U-Pb and Sm-Nd age determinations for monazite and garnet show that the Paleoproterozoic metamorphic cycle took place at 1.84–1.79 Ga, related with thrusting of the Lapland granulites onto the adjacent terranes and subsequent exhumation.

Keywords: Archean; Paleoproterozoic; metamorphism; age determination; Fennoscandian Shield; Finland

1. Introduction

The Archean bedrock in the northwestern part of the Fennoscandian Shield has a prolonged tectonic history of nearly two billion years from Paleoproterozoic to Paleoproterozoic. During the Proterozoic Svecofennian orogeny at 1.92–1.77 Ga many parts of the Archean were strongly reworked in collisional processes. The Proterozoic rocks overthrust onto the Archean craton and the Archean crust was in many places heated and deformed in a brittle to ductile manner. Proterozoic mobile belts are found in the Archean crust where granulite or upper amphibolite facies mineral assemblages are overprinted and replaced by Proterozoic mid to low amphibolite facies assemblages [1,2]. Proterozoic deformation and metamorphism have also reset the isotopic systems in many places. In the Karelia Province

(Figure 1), Archean rocks have locally yielded Proterozoic, 1.89–1.77 Ga U-Pb ages on monazite, xenotime and titanite [1–5]. The wall rocks of some shear zone-related Au deposits in the Karelia Province have yielded Rb-Sr ages of c. 1.74–1.72 Ga [6]. In large areas in the western part of the Karelia Province, the K-Ar ages of biotite and hornblende from Archean TTGs and amphibolites are 1.9–1.8 Ga [7], Paleoproterozoic metamorphism having also reset paleomagnetic systems in those areas [8].

Apart from numerous isotope studies, less attention has been paid to the metamorphic petrology of the multiply metamorphosed Archean rocks, which could shed more light on their complex tectonic development and contribute to the models presented for the Paleoproterozoic orogens in the northern Fennoscandia [9]. In this paper, we describe the metamorphic history of the Tuntsa Suite that belongs to the northwesternmost part of the Archean Belomorian Province of the Fennoscandian Shield (Figure 1). Many studies have demonstrated that most parts of the Belomorian Province (Figure 1) underwent intensive Proterozoic metamorphism, which is recorded, for example, by disturbances in the Sm-Nd isotope system and by 1.94–1.77 Ga U-Pb ages on metamorphic zircon, monazite, titanite and rutile from Archean rocks [10–13]. It has been proposed that the Belomorian Province is a mobile belt which had already collided with Karelia in the Neoproterozoic but later was compressed between the Kola and Karelia continents at around 1.91–1.88 Ga [13–16].

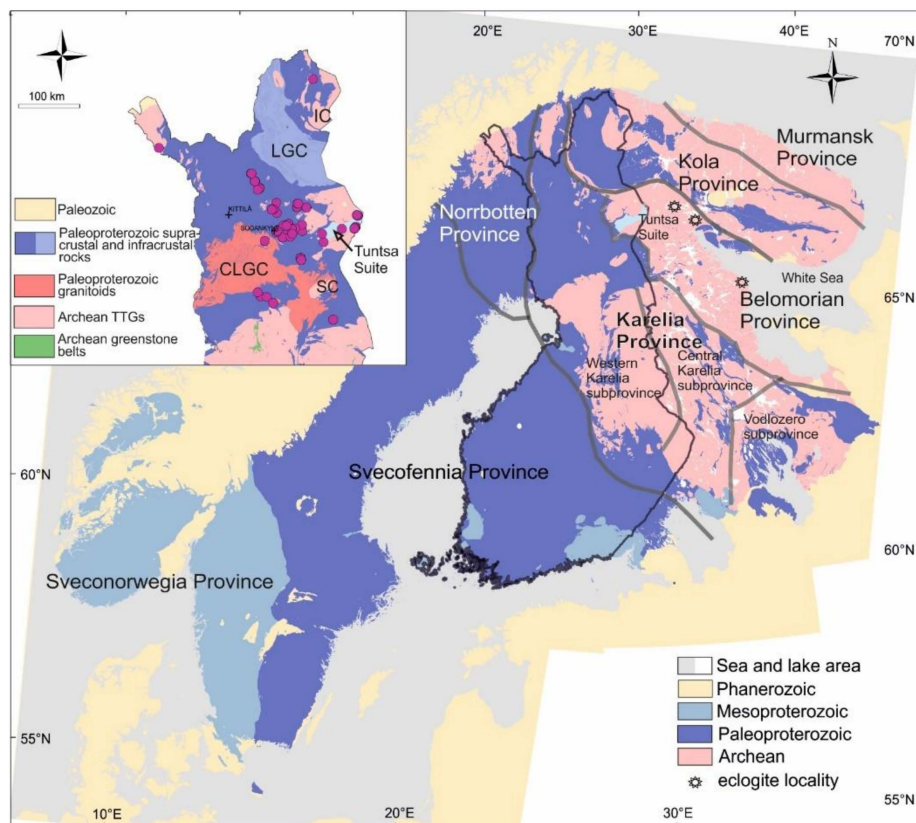


Figure 1. Generalised geological map of the Fennoscandian Shield, simplified from the Geological Map of the Fennoscandian Shield 1:1,000,000 (Electronic resource), Espoo, Geological Survey of Finland (fennoscandia_geology_fin_1m.xml). The land area of Finland is outlined. The Tuntsa Suite is marked with light blue. Eclogites in the Belomorian Province are marked with stars. The inset is a simplified geological map of northern Finland, the red dots show the locations of kyanite-bearing rocks. IC = Inari Complex, LGC = Lapland Granulite Complex, CLGC = Central Lapland Granulite Complex, SC = Suomajärvi Complex. The province boundaries are modified from Nironen [17] and Hölttä et al. [18].

The Tuntsa Suite (Figure 2) mainly consists of metasedimentary rocks, including porphyroblastic garnet-, staurolite- and kyanite-bearing metapelitic gneisses that show evidence of multiple metamorphisms. In this paper we document for the first time the strong effect of Proterozoic metamorphism not only on the isotopic ages but also on mineral assemblages and mineral compositions in these gneisses, using Scanning Electron Microscopy (SEM) and electron probe mineral analysis (EPMA), phase equilibria modelling and zircon, monazite and garnet geochronometers.

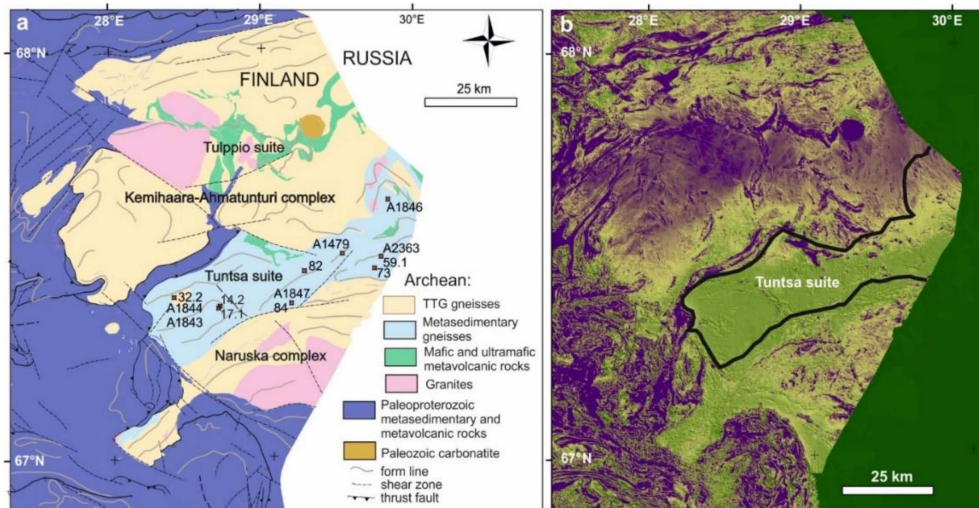


Figure 2. (a) Lithological map of the Tuntsa Suite and surrounding areas, simplified from Bedrock of Finland – DigiKP, Digital map database (Electronic resource). Espoo: Geological Survey of Finland (bedrock_of_finland_200k.xml); (b) pseudocolour magnetic map, purple = magnetic maximum, green = magnetic minimum, the Tuntsa Suite outlined. In (a) the dots with numbers refer to the sites of the studied samples (TTKI-2005-14.2-84).

2. Geological Setting

2.1. Fennoscandia

The Fennoscandian Shield is comprised of Archean and Proterozoic terrains, the former covering roughly one-third of the Shield area in its NE part. The Archean and overlying Paleoproterozoic rocks (Figure 1) are divided into Norrbotten, Murmansk, Kola, Karelia and Belomorian Provinces which all have distinct geological features and which by definition were components in accretion or collision.

The Karelia Province is divided into the Vodlozero Subprovince in the southeast, the Central Karelia Subprovince in the middle and the Western Karelia Subprovince in the northwest (Figure 1). Important distinctive characteristics of the subprovinces include that, based on existing age determinations, Mesoarchean 3.2–2.8 Ga volcanic rocks and TTGs are common in the Vodlozero subprovince, also being found in the Western Karelia subprovince, whereas granitoids and greenstones in the Central Karelia subprovince are Neoproterozoic, ≤ 2.8 Ga. High-grade metamorphism and partial melting at c. 2.71–2.63 Ga characterizes all provinces, presumably related with the assembly of the Kenorland supercontinent [19,20].

The Belomorian Province east of the Karelia Province mainly consists of 2.93–2.72 Ga TTG gneisses, greenstone belts with volcanic rocks and metasedimentary gneisses. Al-rich metasedimentary gneisses are often kyanite-bearing, and rare orthopyroxene-kyanite assemblages have been found in the Belomorian Province [21,22]. Distinctive features of the Province are eclogites and ophiolite-like volcanic rocks, not discovered elsewhere in the Archean of the Fennoscandian Shield [23]. Reflection seismic studies suggest that the Belomorian Province comprises a stack of eastward dipping subhorizontal nappes and thrusts, being separated from the underlying Karelia Province by a major

detachment zone. These structures have been interpreted to represent collisional thickening during the Paleoproterozoic [24–26].

Neoarchean eclogites, metamorphosed at pressures of 14–19 kbars, have been found at the White Sea coast [12,27,28], and also in the northern parts of the Belomorian Province (Figure 1) where they have been related to the subduction of the Archean oceanic crust [11,29–32]. However, the age of the high-pressure metamorphism is controversial. Eclogites have yielded zircon ages of 2.94–1.76 Ga but the exact age of the eclogite facies metamorphism is difficult to determine because the area underwent several high-grade regional metamorphic events, both in Archean and Proterozoic, which have promoted zircon crystallization [12,28,33–36]. Based on the evaluation of the existing extensive isotopic data on the Belomorian eclogites Mints and Dokukina [36] concluded that the eclogite facies metamorphism took place at 2.82–2.78, related with subduction of the oceanic lithosphere, and was followed by a series of high-grade metamorphic events from 2.74 Ga to 1.89 Ga. However, Proterozoic zircon and garnet in the Belomorian eclogites indicate that the eclogite facies metamorphism could have taken place at 1.92–1.87 Ga [37–43]. This is also supported by the partly eclogitized Paleoproterozoic 2.4 Ga mafic dykes found in the Gridino area unless there were both Archean and Paleoproterozoic eclogite facies events [12,34,44,45].

Between 2.50 and 1.90 Ga, the Archean continent underwent repeated extensional and compressional events, resulting in intracontinental rifting with voluminous deposition of riftogenic volcanic, igneous and sedimentary rocks in the central parts of the craton. Oceans were opened in the present northeast and southwest. In the NE, the ocean separating the Kola and Karelia Provinces was closed at around 1.92–1.91 Ga resulting in collision and thrusting of the Lapland Granulite Complex onto the lower grade rocks in the south. Simultaneously juvenile Paleoproterozoic island arcs and microcontinents together with ophiolite complexes accreted to the Archean continent in the present southwest, partly thrusting onto it. Tectonic thickening led to Barrovian-style metamorphism in the Archean crust and overlying supracrustal rocks [9,16,17,46–55].

In the Central Lapland area, high abundances of granitoids were produced between 1.88–1.77 Ga [51,56,57]. Lahtinen et al. [56] related the c. 1.88 Ga granitoids with the onset of the orogenic collapse after 1.92–1.91 Ga thickening and the youngest granitoids to the final stages of the collapse. In the paragneisses of the Central Lapland area, Lahtinen et al. [51] observed an almost continuous growth of metamorphic zircon from 1.88 to 1.78 Ga which they interpreted as the crust having stayed hot for 100–120 m.y. before final cooling at 1.75 Ga.

2.2. *Tuntsa*

The Tuntsa area comprises the Finnish part of the Belomorian Province in NE Finland (Figure 1). The main units of the area are the metasediment-dominated Tuntsa Suite, the metavolcanic Tulppio Suite and surrounding TTG gneiss complexes (Figure 2). In general, although not completely absent, porphyroblastic Al-rich metapelites are rare in the Archean bedrock of Fennoscandia, the Tuntsa Suite and its extension to the southeast in the Belomorian Province being an exception [21,22].

In the Tuntsa Suite, metasedimentary gneisses are strongly foliated medium-grained metapelites and metapsammites, the former typically containing large staurolite, kyanite and garnet porphyroblasts (Figures 3 and 4). Rocks are weathered and greyish brown on the surface. The primary sedimentary textures have normally been destroyed by the orientation of penetrative foliation. Gneisses are commonly migmatized, and anatectic gneissose granites containing enclaves and ghost-like relics of metasedimentary gneisses are common [58]. Leucosome veins may be up to several vol. %, indicative of partial melting. The thickness of the leucosome veins varies from <2 cm to more than ten centimetres, and they are locally broken and boudinaged (Figure 3c,d). In thin sections, millimetre-scale gneissic banding can be seen where micas and quartz + plagioclase are segregated in separate bands.

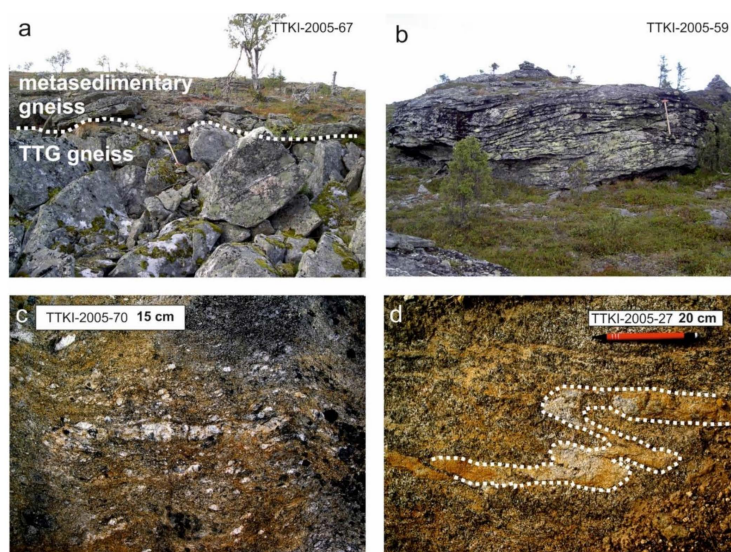


Figure 3. Structures in the Tuntsa gneisses. The exposure code and the length of the bar are given in the inset of each figure; map coordinates are given in Supplementary Materials, Table S1. (a) subhorizontal foliation (S2) in a metasedimentary gneiss which overlies a TTG gneiss. The tectonic contact (marked with a white dotted line) is above the hammer in the middle of the photograph; (b) a typical late subhorizontal S2 foliation in a metasedimentary gneiss; (c) fractured leucosomes in a staurolite- and kyanite-bearing gneiss showing the S2 foliation; (d) folded leucosomes (emphasized with white dotted lines) in staurolite-bearing metasedimentary gneiss.

In the NW part of the Tuntsa Suite within the metasedimentary gneisses, there are amphibolites and amphibole-chlorite schists. Thin mafic dykes are found in its southern and western parts, and in the northern part ultramafic intrusions and gabbro dykes are common. In the central and northern parts of the Tuntsa Suite there are numerous tourmaline-bearing granite pegmatite dykes [59].

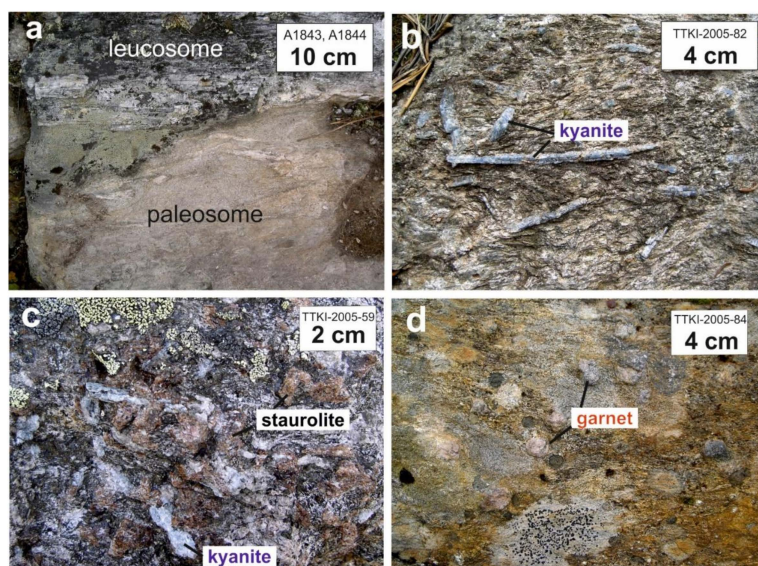


Figure 4. Photographs of the Tuntsa metasedimentary gneisses and porphyroblasts. (a) deformed paleosome and leucosome (nomenclature after Sawyer [60]) in the exposure TTKI-2005-32, sampled for age determinations; (b) kyanite crystals in cordierite-bearing gneiss; (c) staurolite and kyanite grains in the exposure shown in Figure 3b, (d) big garnet grains in metasedimentary gneiss.

Based on field relationships and previous age determinations [59] the Tuntsa metasedimentary suite seems to be at the border between two Archean TTG terranes of different age. To the north of

the Tuntsa Suite within the Kemihaara-Ahmatunturi granitoid complex, TTG gneisses yield U-Pb zircon ages of 2.85–2.80 Ga. Tonalite of this age also cross-cuts metavolcanic rocks of the Tulppio Suite. South of the Tuntsa Suite, within the Naruska granitoid complex TTG gneisses are younger and were dated at 2.75–2.70 Ga. A mafic dyke in the Naruska complex was dated at 1.94 Ga. Titanites yield both Archean and Proterozoic U-Pb ages, and slightly discordant monazite from a granite north of the Tuntsa Suite gives a U-Pb age of 1.90 Ga [59]. From the supracrustal rocks of the Tuntsa Suite there are no previously published age data.

2.3. Deformation

A distinctive structural feature in the Tuntsa Suite is the strong penetrative flat-lying foliation (Figure 3b) that commonly has obliterated both the primary sedimentary structures and migmatite structures of the gneisses. For example, leucosome veins in metasedimentary gneisses have been broken into smaller fragments (Figure 3c). The general strike of foliation (S2) in the western part of the suite is to the ENE, mostly with a gentle dip of 5–30° to the NNW. In the NE part of the Suite, there is open folding with NE striking axial plane; this folding can be also seen in the aeromagnetic map north of the Tuntsa Suite in the Kemihaara-Ahmatunturi complex (Figure 2a,b). A detailed structural analysis covering the whole Tuntsa Suite is lacking, but Juopperi and Veki [61] described in a small area in the eastern part of the Tuntsa Suite four main stages of deformation. According to their observations, the first phase D1 is characterized by upright isoclinal folding which has penetrative axial plane cleavage. D2 was regional and characterized by reorientation of isoclinal F1 folds into gently dipping positions, tight F2 folding and development of a strong axial plane S2 foliation. This deformation is the strongest and can be seen all over the Tuntsa Suite (Figure 3a,b). According to Juopperi and Veki [61], the third deformation phase D3 is characterized by E-W trending kink or chevron type folding with crenulation cleavage in the axial plane; these kind of D3 structures are also common elsewhere in the Tuntsa Suite. The fourth deformation phase D4 is represented by ENE trending open folding with weak fracturing in the axial plane.

3. Analytical Methods

3.1. Microprobe Analyses

Microprobe analyses were carried out at the Geological Survey of Finland (Espoo, Finland) using a CAMECA SX-100 electron microprobe. The beam width was 5 µm, the sample current was 20 nA and the acceleration voltage was 15 kV. Natural standards and the ZAF correction program were used. Selected mineral analyses are presented in Supplementary Materials, Table S2.

3.2. Whole-Rock Analyses

The whole-rock compositions were analysed from thin section cut-offs and fist-size hand specimens in the laboratory of Labtium Co. (Espoo, Finland) using the X-ray fluorescence technique (WD-XRF) from pressed pellets (<https://labtium.fi/en/our-services/exploration-and-mining/exploration-petrological-analyses/>).

3.3. SEM Analyses

Monazite grains were detected by scanning the thin sections using the scanning electron microscope (SEM) model JEOL JSM5900 LV at the Geological Survey of Finland (Espoo, Finland). The SEM was equipped with an energy dispersive X-ray spectrometer (EDS) with INCA Feature phase detection and classification software to characterize grain size, shape and mineralogical composition of particular materials. Back-scattered electron images (BSE) images were taken from monazite and zircon grains to find the possible zoning and to target the analysis spots.

3.4. QEMSCAN Imaging

The mineralogy of the selected samples was analysed by automated scanning electron microscopy with energy dispersive spectrometers (SEM-EDS), using a QEMSCAN[®] 4300, at the Camborne School of Mines, University of Exeter, UK [62,63]. The samples were measured using Fieldscan Mode (iMeasure software) and the resulting data processed using iDiscover image analysis software [64,65].

The entire area of each thin section was measured at an X-ray resolution of 10 microns, with areas of interest scanned at 1 micron X-ray resolution. Data processing and database development was required due to the specialist nature of the samples, which involved adding, and improving SIP (database) categories to match the samples, producing a customised database. Although all the minerals were checked, specific attention was paid to the chlorite, cordierite, garnet and tourmaline categories, as these have similar or overlapping compositions [66]. Therefore, validation by optical petrology and manual SEM was required, with multiple iterations of changes and checks. All four minerals may contain varying concentrations of Fe, Al, Si, with or without Mg, thus this variability combined with the 1,000 count spectra used by QEMSCAN [66,67], means that they can be difficult to separate. A combination of elemental abundance, elemental ratios, BSE and boundary phase processing was used to distinguish them. Mapping of the compositional zoning within individual garnet grains was achieved by using the detected Fe, Al, Ca and Si proportions, in combination with BSE greyscale values. Modal mineralogy, mineral association, average grain size and mineral maps were output for each of the samples (Supplementary Materials, Table S3).

3.5. Isotope Analyses

Zircon, monazite and garnet were dated using the secondary ion mass spectrometry (SIMS), laser ablation inductively coupled plasma mass spectrometry (LA-ICP-MS) and thermal ionization mass spectrometry (TIMS); the reason for the usage of many instruments was that the isotopic analyses were completed over a decade and new facilities became available during the work. The analytical data are presented in Supplementary Materials, Table S6.

Sample preparation and procedures for the TIMS U-Pb and Sm-Nd analyses follow those described by Huhma et al. [68,69]. Isotopic ratios were corrected for fractionation, blank and age related common lead according to Stacey & Kramers [70]. Chemical abrasion followed the method by Mattinson [71].

Zircon grains from the sample A1843 were analyzed using the Nordic Cameca IMS 1270 ion microprobe at the Swedish Museum of Natural History, following methods described by Whitehouse & Kamber [72].

For the LA-ICP-MS analyses, two mass spectrometers at the Geological Survey of Finland in Espoo were used. Separated zircon grains from the samples A1846 and A1479 were analysed using the Nu Plasma II multi-collector ICP-MS coupled with Photon Machine Analyte G2 laser. Grains were ablated in He gas (gas flows = 0.4 and 0.1 L/min) within a HelEx ablation cell [73]. The He aerosol was mixed with Ar (gas flow = 0.8 L/min) before entry into the plasma. The gas mixture was optimized daily for maximum sensitivity. All analyses were carried out in static ablation mode. Ablation normal conditions were: beam diameter: 20 µm, pulse frequency: 5 Hz, beam energy density: 0.55 J/cm². Measurements were made using the GJ1 (609 Ma) and A1772 (2712 Ma) standards. Data quality is regularly monitored by analyses on a control sample with known age (A382). Data reduction was performed off-line, using an interactive spreadsheet program written in Microsoft Excel/VBA by T. Andersen [74].

The U-Pb analyses on monazite of the samples TTKI-2005-82, TTKI-2005-14.2, TTKI-2005-32.2, TTKI-2005-59.1 and TTKI-2005-73 were performed from normal 30 µm thick polished sections, using a Nu Plasma AttoM single collector ICPMS connected to a Photon Machine Excite laser ablation system. Zircons from the sample A1843 were also analysed using the AttoM. Typical ablation conditions were: beam diameter: 15 µm for monazite and 25 µm for zircon, pulse frequency: 5 Hz, beam energy density: 2 J/cm². An age-related common lead correction was used when the analysis showed common lead contents significantly above the detection limit (i.e., >50 cps). In-house standards A49 (monazite)

and A382 (zircon) were run at the beginning and end of each analytical session, and regular intervals during sessions.

Raw data were corrected for the background, laser-induced elemental fractionation, mass discrimination and drift in ion counter gains and reduced to U-Pb isotope ratios by calibration to concordant reference zircons, using the program Glitter [75]. Plotting of the U-Pb isotopic data and age calculations were performed using the Isoplot/Ex 4.15 software [76].

3.6. Mineral Equilibria Modelling

The pseudosections were constructed using the Perple_X 6.8.9 software [77,78] (<http://www.perplex.ethz.ch/>) with the thermodynamic data of Holland & Powell [79]. The used activity models were by Holland and Powell [80] for feldspar (Pl(I1, HP)) and by White et al. [81] for other minerals (Gt(W), Mica(W), Chl(W), St(W), Crd(W), Bi(W), Ilm(WPH) in the Perple_X solution model file).

4. Samples

The petrography was studied from 68 thin sections sampled from metapelitic gneisses in the Tuntsa Suite. Mineral analyses were done from 15 porphyroblastic samples, selected analyses are presented in Supplementary Materials, Table S2. Five samples were collected for zircon U-Pb age determinations from separated mineral fractions. Sm-Nd whole-rock analyses were also done from these samples. Monazite was analysed from six samples, five of these were thin sections and the sixth was a mineral separate. Six thin sections were analysed using the scanning electron microscope and four of these were selected for pressure-temperature (PT) modelling and monazite dating, based on their regional distribution and of compositional differences in garnet. Detailed description of the samples are given in Supplementary Materials S7.

4.1. Samples for Zircon Analyses

A1843 is from a typical metapelitic gneiss in Tuntsa, comprising biotite, plagioclase, quartz, garnet, staurolite, kyanite, chlorite, sericite, tourmaline and ilmenite. Chlorite and sericite are fine-grained alteration products of garnet and staurolite, and some of the Chl+Ser may be pinitized cordierite (cf. TTKI-2005-32.2 in Figure S4). The zircon age determinations were expected to give constraints both to metamorphism and to the maximum age of sedimentation. Zircon was found but monazite was not obtained from the sample A1843.

A1844 is from felsic, strongly deformed concordant vein from the same exposure as A1843, with a thickness of several tens of centimetres. It was interpreted to be a leucosome (Figure 4a), in which case at least some zircon was expected to have been crystallized from the leucosome melt, giving the age of melt crystallized during the high-grade metamorphism. The mineral association was quartz, plagioclase, tourmaline, kyanite and chlorite-sericite intergrowths that are pseudomorphing another mineral, presumably cordierite. A small amount of monazite was obtained from A1844 but no zircon was found.

A1846 is from a trondhjemitic gneiss within the metasedimentary rock, classified as trondhjemite based the whole-rock composition. It comprises plagioclase, quartz and biotite. The latter was partly altered into muscovite and chlorite. The contacts are not exposed and the gneiss is strongly deformed but as a working hypothesis, it was interpreted to be an intrusion into the sediment in which case the deposition of the sediment should be older than the trondhjemite. The sample provided lots of zircon but not monazite.

A1847 is from an intermediate gneiss interpreted to be a metavolcanic rock. The mineral association is hornblende, biotite, plagioclase and quartz, amphibole being locally altered into chlorite. It forms a few tens of metres thick interlayer in the metasedimentary rock, interpreted to be coeval with the sedimentation. Unfortunately, A1847 did not provide either zircon or monazite but Sm and Nd isotopes were analysed from the whole rock sample.

A1479 is from a tourmaline-bearing pegmatite. The main minerals are plagioclase, quartz, tourmaline and muscovite. According to Juopperi (pers. comm.), the pegmatite crosscuts metasedimentary rocks, amphibolites and ultramafic rocks, therefore it was expected to give a minimum age for metamorphism and mafic magmatism. The sample provided a few zircon grains but not monazite.

A2363 is a metapelitic gneiss comprising garnet, biotite, staurolite, kyanite, chlorite, plagioclase and quartz. In this sample, garnet was dated using the Sm-Nd method. The thin section TTKI-2005-59.1, used for PT modelling was from the same sample.

4.2. Samples for SEM Imaging, PT Modelling and Monazite Analyses

Six thin sections were selected for QEMSCAN imaging based on microprobe analyses that showed strong zoning in some garnet grains and weak zoning in others. Based on mineral assemblages and regional distribution, four of these were chosen for PT modelling (TTKI-2005-14.2, TTKI-2005-32.2, TTKI-2005-59.1, TTKI-2005-73). Monazite also was analysed from these four thin sections and also from sample TTKI-2005-82. The details and petrography of the samples are described in Supplementary Materials S7.

5. Results

5.1. Petrography of the Metapelitic Gneisses

A list of the samples collected in this work with their mineral associations and sampling site map coordinates is presented in Supplementary Materials, Table S1. A typical association in the metapelitic gneisses is staurolite-biotite-quartz-plagioclase ± garnet ± kyanite ± chlorite ± cordierite ± muscovite. The grain size of quartz, biotite and plagioclase in the matrix is mainly <2 mm, while the porphyroblastic minerals may be up to several centimetres in diameter (Figure 4). Staurolite is the most common porphyroblast, the others in order of frequency are garnet, kyanite, cordierite, sillimanite and andalusite (the least common).

From the studied thin sections andalusite was found in two localities and sillimanite in four outcrops, both minerals in the eastern part of the study area. However, Juopperi [58] reported sillimanite also in the western part of the Tuntsa Suite, therefore the Al-silicates probably do not have any systematic regional distribution. Kyanite and fibrolitic sillimanite were occasionally found together in the same thin section. Chlorite is common but prograde muscovite is rare, sericite is common in retrograded pseudomorphs where it replaces staurolite, kyanite and andalusite. Common accessories are tourmaline, zircon, apatite, rutile, ilmenite, pyrrhotite and pyrite.

Staurolite is found as idiomorphic and subidiomorphic poikiloblastic grains whose size is mostly <5 mm but larger grains are also found.

Garnet porphyroblasts are found as two main textural types, named here A and B types. Normally in a thin section, only one type was found. A-type garnet is euhedral and texturally zoned having a core with quartz, plagioclase, biotite, chlorite, ilmenite and commonly abundant dusty opaque inclusions and an inclusion-free rim (Figures 5c and 6). The grain size is normally <3 mm. Locally the core is poikiloblastic having inclusions that are mostly quartz and plagioclase. B-type garnet forms subhedral, strongly poikiloblastic grains whose size is bigger than that of the A-type garnet. They have inclusion trails, mostly comprising quartz + plagioclase, that are often curved (Figure S4). Dusty opaque inclusions are also common; at the edges of garnet grains the abundance of inclusions increases, with the rims looking dark in thin section. The larger garnet grains (>3 mm) of both textural types are altered from fractures into biotite and sericite. Euhedral small garnet grains are also found as inclusions in staurolite and andalusite (Figure 5b,c).

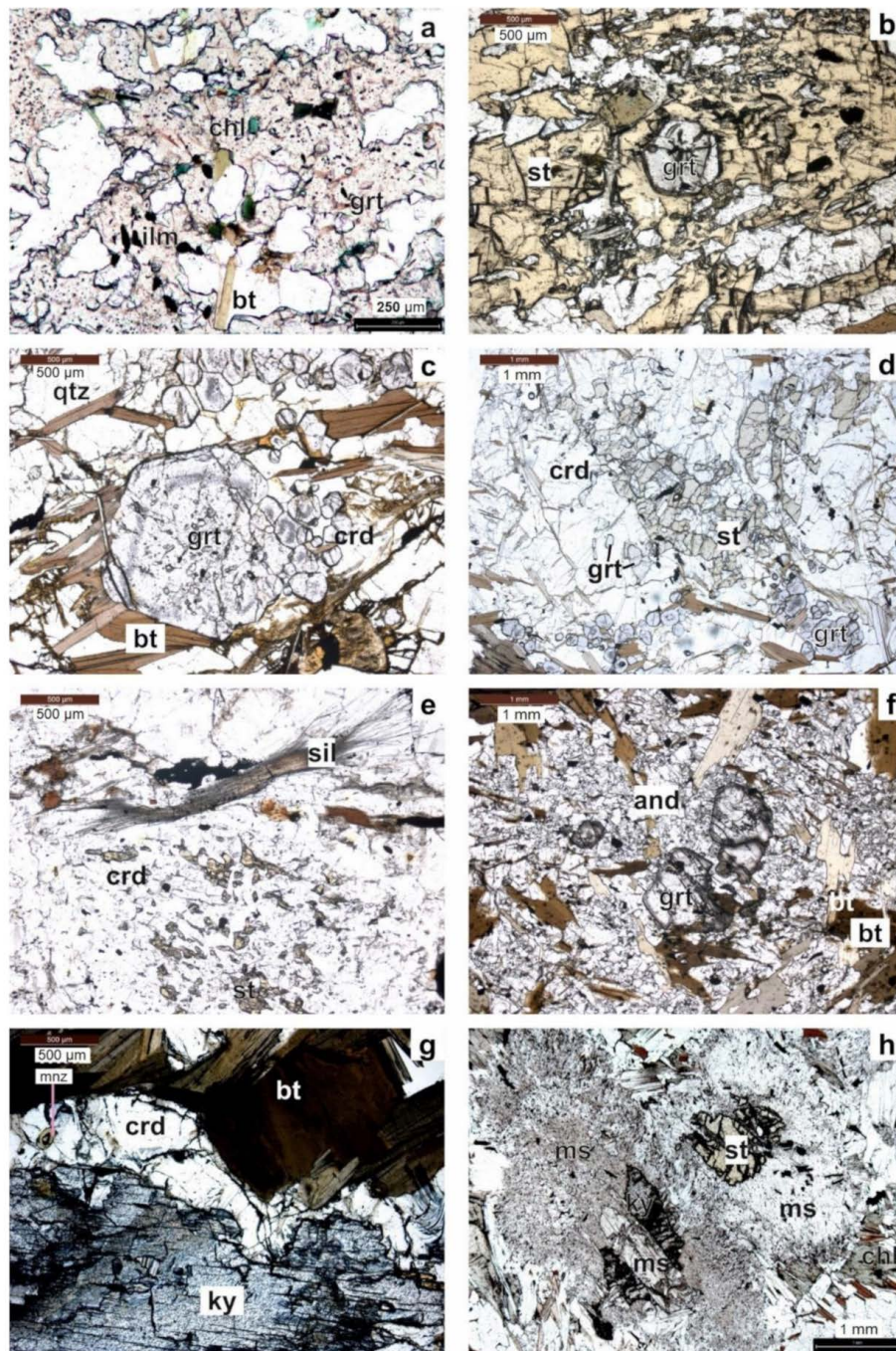


Figure 5. Microphotographs (parallel nicols) of metamorphic textures. (a) chlorite, biotite and ilmenite inclusions in garnet, TTKI-2005-40.3; (b) A-type garnet inclusion in staurolite, TTKI-2005-49.1; (c) euhedral A-type garnet in the thin section TTKI-05-31.2; (d) decomposing staurolite, forming cordierite and euhedral garnet; TTKI-2005-31.2; (e) staurolite inclusions in cordierite overgrown by fibrolitic sillimanite, TTKI-05-79.2; (f) euhedral garnet surrounded by andalusite, TTKI-05-72.2; (g) cordierite corona with monazite inclusions between kyanite and biotite, TTKI-05-82 (Figure 4b); (h) kyanite and staurolite altering into muscovite and chlorite, TTKI-2005-70.1. bt = biotite; grt = garnet; chl = chlorite; st = staurolite; qtz = quartz; crd = cordierite; and = andalusite; ky = kyanite; mnz = monazite, ms = muscovite.

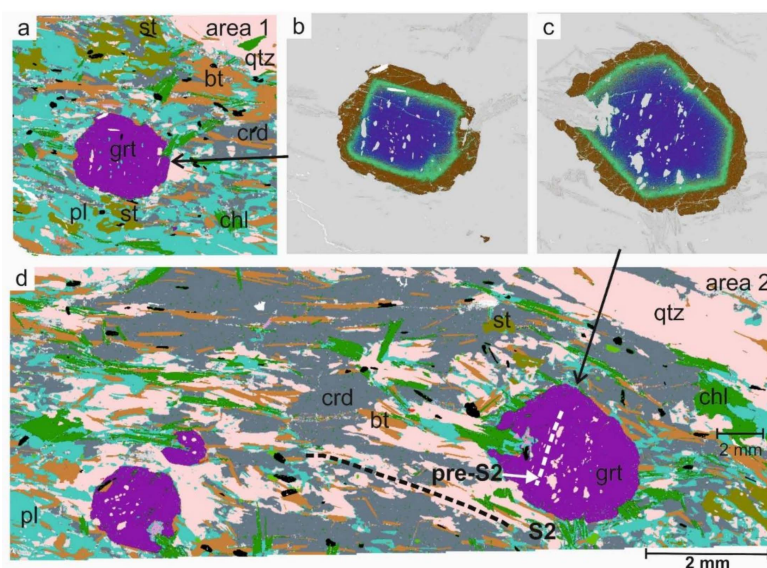


Figure 6. QEMSCAN images of A-type garnet in the thin section TTKI-2005-14.2. The image of the whole thin section is shown in Supplementary Materials Figure S4. (a) False colour QEMSCAN mineral map showing a garnet and matrix. (b) False colour QEMSCAN mineral map showing the zoning in the garnet from image (a). (c) False colour QEMSCAN mineral map showing the zoning in the garnet from image (d). (d) False colour QEMSCAN mineral map showing the S2 foliation in the matrix and garnet from image (c) For the compositional differences, causing the zoning in the two upper right figures, see Figure 7.

Cordierite is typically anhedral and elongated along schistosity. It occurs both as strongly pinitized and unaltered grains. As in other porphyroblasts quartz, biotite and opaque minerals are common inclusions. Quartz and cordierite form symplectitic intergrowths. Staurolite commonly occurs as inclusions in cordierite (Figures 5 and 6) that also forms coronas on staurolite, indicating that much of cordierite was formed in a staurolite decomposition reaction. Cordierite also forms reaction rims between kyanite and biotite (Figure 5g).

Kyanite is idiomorphic and commonly elongated along schistosity, the biggest grains being up to 6–7 cm in length (Figure 4b). Medium-grained kyanite is less poikiloblastic, but with increasing grain size quartz and micas are found as inclusion trails. Kyanite and staurolite as well as kyanite and garnet are found in contact (Supplementary Materials, Figure S4). Other Al_2SiO_5 polymorphs are rare, but locally *andalusite* is found as up to ~1 cm anhedral poikiloblastic grains with inclusions of garnet, quartz, biotite, muscovite and opaque minerals (Figure 5f). *Sillimanite* is always fibrolitic and in most cases, it is crystallized on biotite rims. The mutual relationships of the Al-silicates were not seen in the thin sections. However, sillimanite is overgrowing cordierite (Figure 5e), indicating that it is a later phase than kyanite.

5.1.1. Textural and Paragenetic Relationships

Early Assemblages

The earliest mineral assemblages in metapelitic rocks are presumably those that form inclusion trails in garnet, being at a high angle with the dominant S2 foliation (Figure 6). The inclusion trails mostly consist of quartz and plagioclase but within many garnet grains, there are also tiny ilmenite, chlorite, biotite and sometimes muscovite inclusions in those trails suggesting that the early (pre-D2) paragenesis in many rocks was Grt-Bt-Chl-Pl-Qtz-Ilm-Ms (mineral abbreviations after Kretz [82]).

Peak Assemblages

The parageneses that crystallized during the highest temperature and corresponding pressure is considered as the peak assemblage. This stage is characterized by coarse-grained garnet, kyanite and staurolite. They are commonly in textural equilibrium (Figure 4, Supplementary Materials, Figure S4), so the stable assemblages were St-Ky-Bt-Pl-Qtz±Grt±Chl, St-Bt-Pl-Qtz±Grt±Chl, Grt-Bt-Pl-Qtz and Ky-Bt-Pl-Qtz. Staurolite seldomly has garnet inclusions (Figure 5b).

Late Assemblages

The late stage of metamorphism is characterized by decompression reactions where garnet and staurolite partly decomposed forming commonly cordierite and seldomly andalusite. Cordierite has commonly staurolite inclusions, garnet inclusions were observed in andalusite (Figure 5f). In Mg-rich metapelitic rocks cordierite rims developed between kyanite and biotite (Figure 5, Figure S4). New, compositionally different garnet crystallized on the rims of old euhedral garnet grains (Figure 6). The parageneses were Grt-Crd-Bt-Pl-Tur-Qtz±Chl, Crd-Bt-Qtz and Bt-Pl-Qtz-And. Chlorite may have been stable at this stage but partly it may be even later. In the latest cooling stage kyanite was altered into muscovite, biotite and staurolite were altered into chlorite and muscovite (Figure 5h) and cordierite was pinitized. The latest parageneses are Ms-Pl-Qtz and Chl-Pl-Qtz±Ms±Bt. Muscovite and chlorite often overgrow biotite as randomly oriented flakes. Chlorite is in some samples rather abundant, found in S2 cleavage planes but rare in the others found as randomly oriented flakes (Supplementary Materials Table S3 and Figure S4). Therefore it is not quite clear if chlorite was stable also during the highest T or if it is all retrograde. For the analysed chlorites, the chlorite thermometer by Bourdelle and Cathelineau [83] yielded temperatures of 274–415 °C which support the latter alternative (Supplementary Materials, Table S2).

5.1.2. Mineral Chemistry

The two textural *garnet* types also have different compositional characteristics, also shown by the QEMSCAN imaging (Figures 6 and 7). Most analysed grains have a composition where the X_{Ca} (Ca/Fe+Mn+Mg+Ca) and the X_{Mn} (Mn/Fe+Mn+Mg+Ca) decrease and the X_{Mg} (Mg/Fe+Mn+Mg+Ca) increases from the core to rim. In the euhedral A-type garnet that has inclusion-free rims, this change is in some grains very abrupt at the core-rim boundary. Especially in the textural type B, forming subhedral, strongly poikiloblastic grains the zoning is smoother (Figure 7, Supplementary Materials, Figure S4). The X_{Ca} is quite high in cores of many garnet grains, up to 0.14–0.19, and the X_{Mg} increases in zoned grains from c. 0.06–0.08 in the core to 0.15–0.16 in the rims. Ca and Mn zoning in the sample TTKI-2005-32.2 is weak, relatively Mg-rich throughout the grain.

Staurolite is Fe-rich, X_{Fe} (Fe/Fe+Mn+Mg+Zn) varying from 0.90–0.81. Staurolite has usually quite low ZnO content, 0.10–0.40 wt.%, but in three staurolite grains ZnO is more abundant, 1.11–1.79 wt.%. Cr₂O₃ is low, <0.3 wt.%. The analysed grains do not show significant Zn and Cr zoning.

Cordierite has generally an X_{Mg} (Mg/Mg+Fe) from 0.67 to 0.70. In cordierite from the sample TTKI-2006-82 the X_{Mg} is 0.78, but the whole rock composition in this rock is also Mg-richer than in other analysed rocks. Cordierite has a low CaO content, <0.03 wt.%. Na₂O content is from 0.16 to 0.94 wt.%.

Biotite has mostly an X_{Mg} (Mg/Mg+Fe) of 0.41 to 0.67, being mainly between 0.50–0.60. Al₂O₃ varies from 18.23–19.66 wt.%. TiO₂ content is from 1.07–2.08 wt.%. Most biotite grains have minor abundances of MnO, 0.01–0.12 wt.%.

Muscovite has a Si content of c. 6.20 p.f.u. The FeO and MgO contents are low, 0.58–0.72 and 0.46–0.54 wt.%, respectively. Na₂O is from 1.02–1.39 wt.% and the X_{Na} (Na/Na+K) is between 0.15–0.19.

Chlorite has FeO of 18.9 to 22.1 wt.%, MgO of 15.6–18.3 and SiO₂ of 24.5–26.2 wt.%. Al₂O₃ is 23.1–23.4 wt.%. The X_{Mg} (Mg/Mg+Fe) is between 0.56–0.63, therefore chlorite is classified as clinocllore. MnO content is 0.12–0.23 wt.% in the analysed grains.

Plagioclase is compositionally mostly oligoclase with X_{Ab} (Na/Ca+Na+K) of 0.69–0.78. The X_{Or} is low, 0.003–0.010.

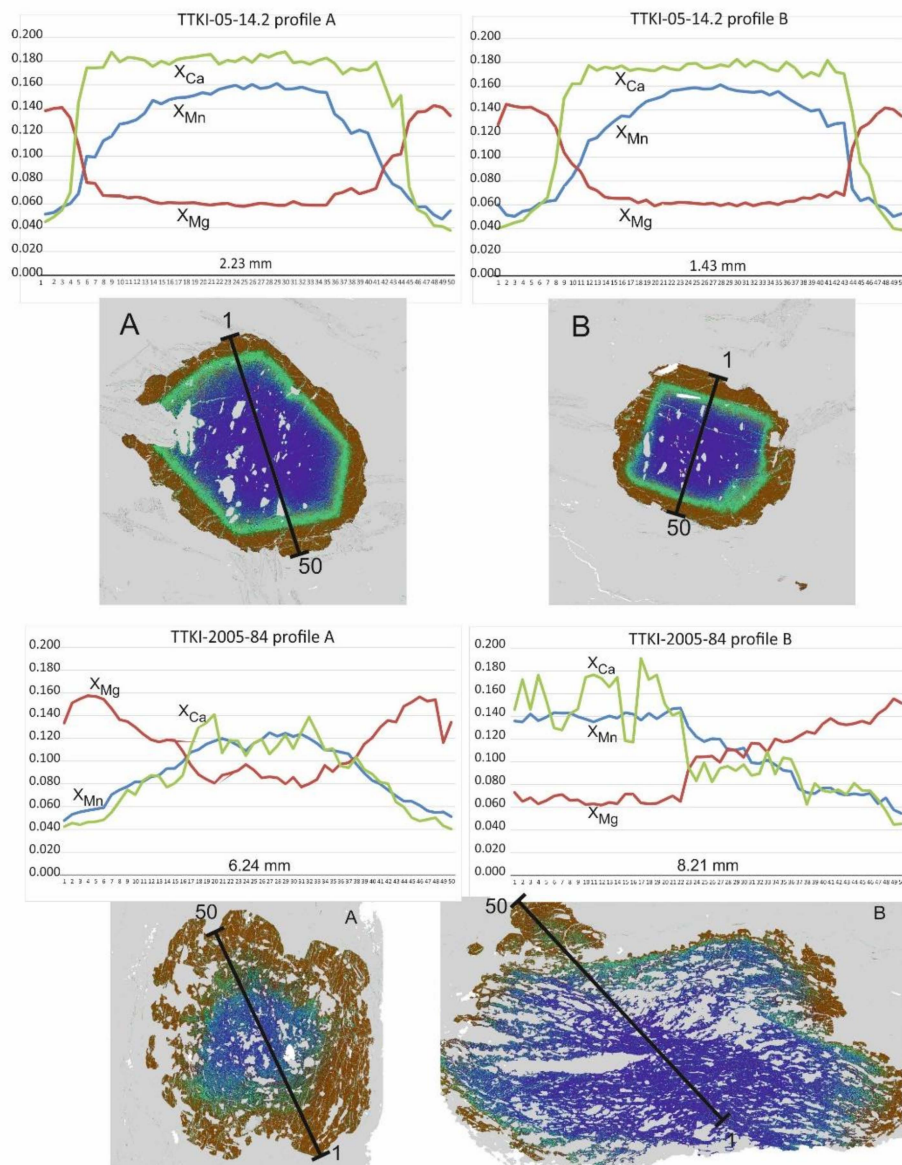


Figure 7. Zoning profiles with QEMSCAN images of the two textural types of garnet grains. Samples TTKI-2005-14.2 (**type A**) and TTKI-2005-84 (**type B**). 50 spots were analysed in every profile. The images of the whole thin sections are shown in Supplementary Materials, Figure S4.

5.2. Zircon Geochronology

Zircon grains in A1843 metapelitic gneiss are mostly dull, short <100 μm long prisms and roundish, oval-shaped crystals where clear oscillatory zoning is not visible in back-scattered electrons (BSE) images. There are also long prisms that show oscillatory zoning, and a few grains that have zoned cores and unzoned rims. The back-scattered electron images of all grains analysed using the SIMS are presented in Supplementary Materials, Figure S5.

The ion microprobe and LA-ICP-MS analytical data are presented in Table S6 and Figure 8. All analyses are from inner domains of the grains, surface fractures were avoided when choosing the spot site. In the Nordsim data (32 analysis spots) the concordant grains fall into two groups, the older grains are 2.84–2.77 Ga and the younger ones mostly from 2.69–2.67 Ga. The LA-ICP-MS data show a continuous spread of concordant $^{207}\text{Pb}/^{206}\text{Pb}$ ages from 2.75–2.50 Ga. The zircon morphology does not

correlate with the age. The youngest, <2.60 Ga, partly discordant grains (disc. % –1 to –8, Table S6) presumably represent Pb loss during the Paleoproterozoic metamorphism. Most zircon grains have low Th and consequently a low Th/U ratio of <0.1, in many analyses only 0.01–0.02, the younger age group mostly yielding the low Th/U ratios (Figure 8).

The $^{207}\text{Pb}/^{206}\text{Pb}$ -age for the discordant TIMS analysis on bulk zircon from A1843 was 2615 Ma (Table S6).

A1846 trondhjemitic gneiss yielded euhedral, long and transparent zircon grains whose crystal edges are slightly rounded. The BSE images show magmatic oscillatory zoning, some grains containing distinct cores. Seven multi-grain TIMS analyses on zircon are slightly heterogeneous and discordant with $^{207}\text{Pb}/^{206}\text{Pb}$ ages of ca. 2.74 Ga. Subsequently, 29 LA-ICP-MS analyses were made on 20 grains (Table S6, Figure 9). Excluding one data point with high common lead, the data are mostly concordant within error and yield two age groups. Eight low-U core domains of zircon are ca. 2.85 Ga, whereas results from rims give ages of ca. 2.75 Ga. Also, many grains without distinct cores give ages of ca. 2.75 and all 20 analyses of this younger group give an average age of 2755 ± 8 Ma, which may be considered as the age of magmatic zircon and age of the rock. Th was not analysed with Analyte G2 laser microprobe.

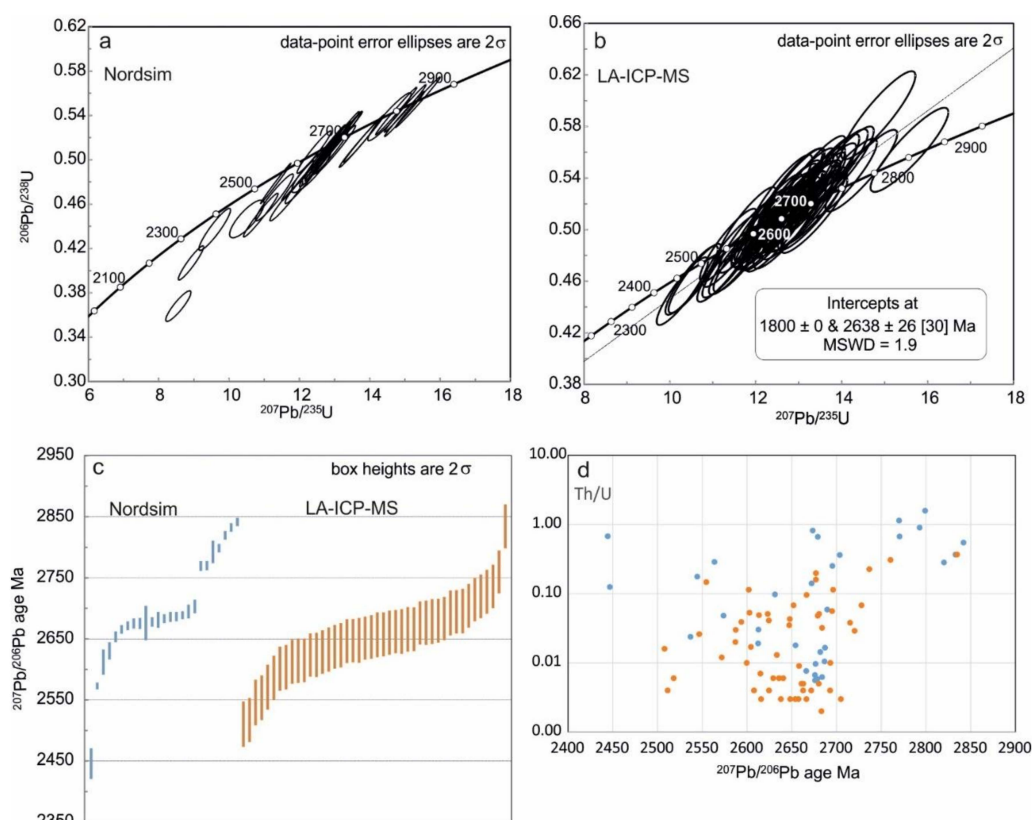


Figure 8. A concordia diagram for zircon grains in the sample A1843, analysed by SIMS (a) and LA-ICP-MS (b); (c) the distribution of the concordant $^{207}\text{Pb}/^{206}\text{Pb}$ ages in Ma; (d) Th/U ratios of the analyzed zircon grains, blue dots = SIMS data, orange dots LA-ICP-MS data.

Pegmatite A1479 yielded only a few zircon grains. Zircon population is heterogeneous and in the BSE images, various domains and cracks are visible. The LA-ICP-MS data obtained on fourteen carefully selected clean domains are of good quality and provide a large range of concordant ages from 2.95 to 1.83 Ga (Table S6, Figure 9). Most grains are Archean and probably derived from the country rock of the pegmatite. Grain 6 has a 2.71 Ga core and distinct high U rim, which yielded an age of ca. 1.82 Ga. These data are too limited to make strong conclusions, but either the pegmatites are Proterozoic or also they were metamorphosed at around 1.83 Ga. The pegmatite lacks the 2.69–2.67 Ga zircon,

indicating that the pegmatite was not crystallized during the Archean high-grade metamorphism of that age.

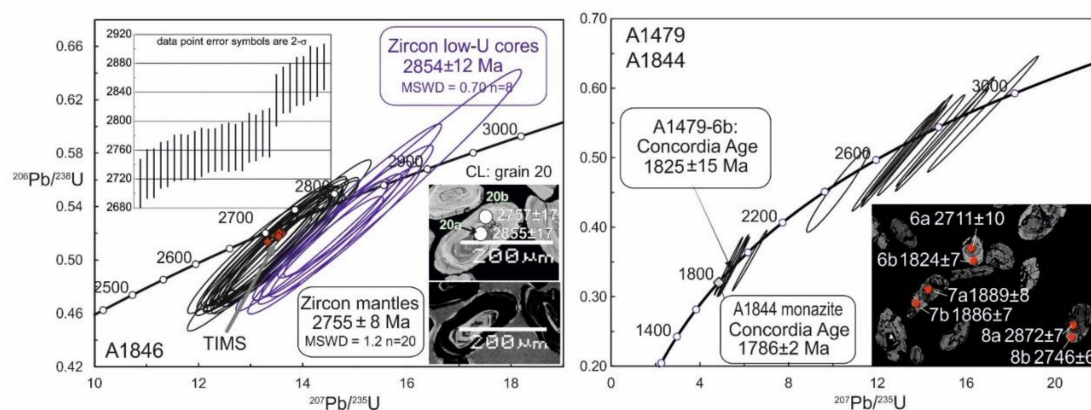


Figure 9. Concordia diagrams for zircon in the trondhjemitic gneiss sample A1846 and the pegmatite sample A1479 and monazite in the leucosome sample A1844. Datapoint error ellipses are 2σ , the blue ellipses are for the older age group grains and the black for the younger. The boxes show the average $^{207}\text{Pb}/^{206}\text{Pb}$ ages for both age groups. The upper left corner inset shows the distribution of the $^{207}\text{Pb}/^{206}\text{Pb}$ ages. The CL image in the lower right corner of the A1846 figure shows the grain 20 (Supplementary Materials, Figure S4) that has a 2.86 Ga core with a 2.76 Ga rim. The CL image in the lower right corner of the A1479–A1844 figure shows the grain 6 (Figure S4) that has an Archean core with a 1.82 Ga rim.

5.3. Monazite Geochronology

The possible zoning of the monazite grains was not visible in the BSE images in any of the samples. In all samples, there were reversely discordant analysis spots that systematically yielded younger ages than concordant spots. This phenomenon is probably related to the analytical error of the laser ablation, as also observed in the large monazite dataset by Hölttä et al. [84]. Therefore the reversely discordant analyses were ignored, and a concordia age could be calculated for all samples (Figure 10). Within the 2σ error, the age is the same for all specimens, 1793–1799 Ma.

In the thin section from the metapelitic rock TTKI-2005-14.2 eleven grains were analysed. Most of them were located at grain boundaries of biotite and quartz but some were also inclusions in main minerals (Figure 11a). The ages fall into two groups that differ within the 2σ error. The concordia age was 1793 ± 9 Ma (2σ , MSWD = 2.2, Figure 10a). The four younger reversely discordant analysis spots yielded an average of $^{207}\text{Pb}/^{206}\text{Pb}$ ages of 1735 ± 20 Ma (MSWD = 0.15). This age is probably meaningless, the reverse discordance caused by analytical errors in the LA-ICP-MS [84]. There is not any significant age difference between the monazite inclusions and those located at grain boundaries.

The TIMS U–Pb analysis of monazite obtained from the sample A1844 from leucosome is concordant within error, providing an age of 1786 ± 2 Ma (Table S6, Figure 9). In the paleosome thin section TTKI-2005-32.2, taken from the same exposure as A1844, the SEM scan found thirteen grains that were large enough for the LA-ICP-MS analyses (≥ 20 μm in diameter). Monazites yielded a spread of $^{207}\text{Pb}/^{206}\text{Pb}$ ages from 1.84–1.74 Ga but again the youngest grains are somewhat above the concordia. The seven concordant or slightly discordant spots yielded a concordia age of 1799 Ma within the 2σ error (Figure 10b). Most monazite grains were from the strongly pinitized area in the thin section (Figure 11c).

In the sample TTKI-2005-59.1 most analysed spots were concordant or only a slightly discordant. The concordia age for 10 analysis spots was 1795 ± 10 Ma (MSWD = 6.1, Figure 10c). In the thin section TTKI-2005-73 only seven grains were found that were large enough for analyses. The $^{207}\text{Pb}/^{206}\text{Pb}$ ages of the four concordant spots differ, the oldest grain being 1.83 Ga and the youngest 1.77 Ga, however,

the age difference is within the 2σ error limits. The concordia age is 1799 ± 30 Ma (MSWD = 1.6, Figure 10d). Six concordant monazite grains in the sample TTKI-2005-82 were of the same age within the 2σ error, yielding a concordia age of 1797 ± 9 Ma (MSWD = 0.87) (Table S6, Figure 10e).

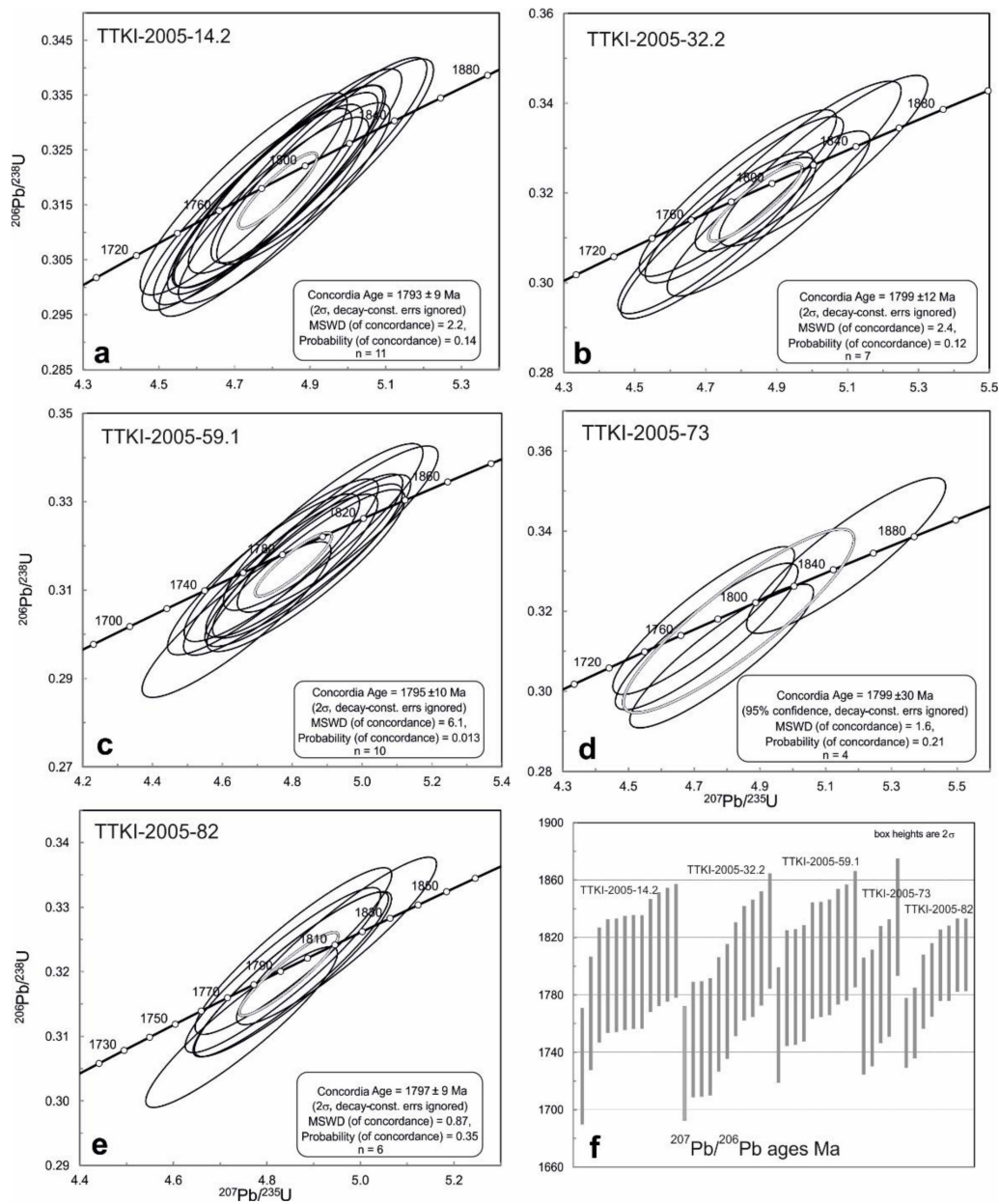


Figure 10. Concordia diagrams for monazite dated using the LA-ICP-MS (a–e) and the $^{207}\text{Pb}/^{206}\text{Pb}$ ages of the analysis spots that were concordant within the 2σ error (f). Data-point error ellipses are 2σ .

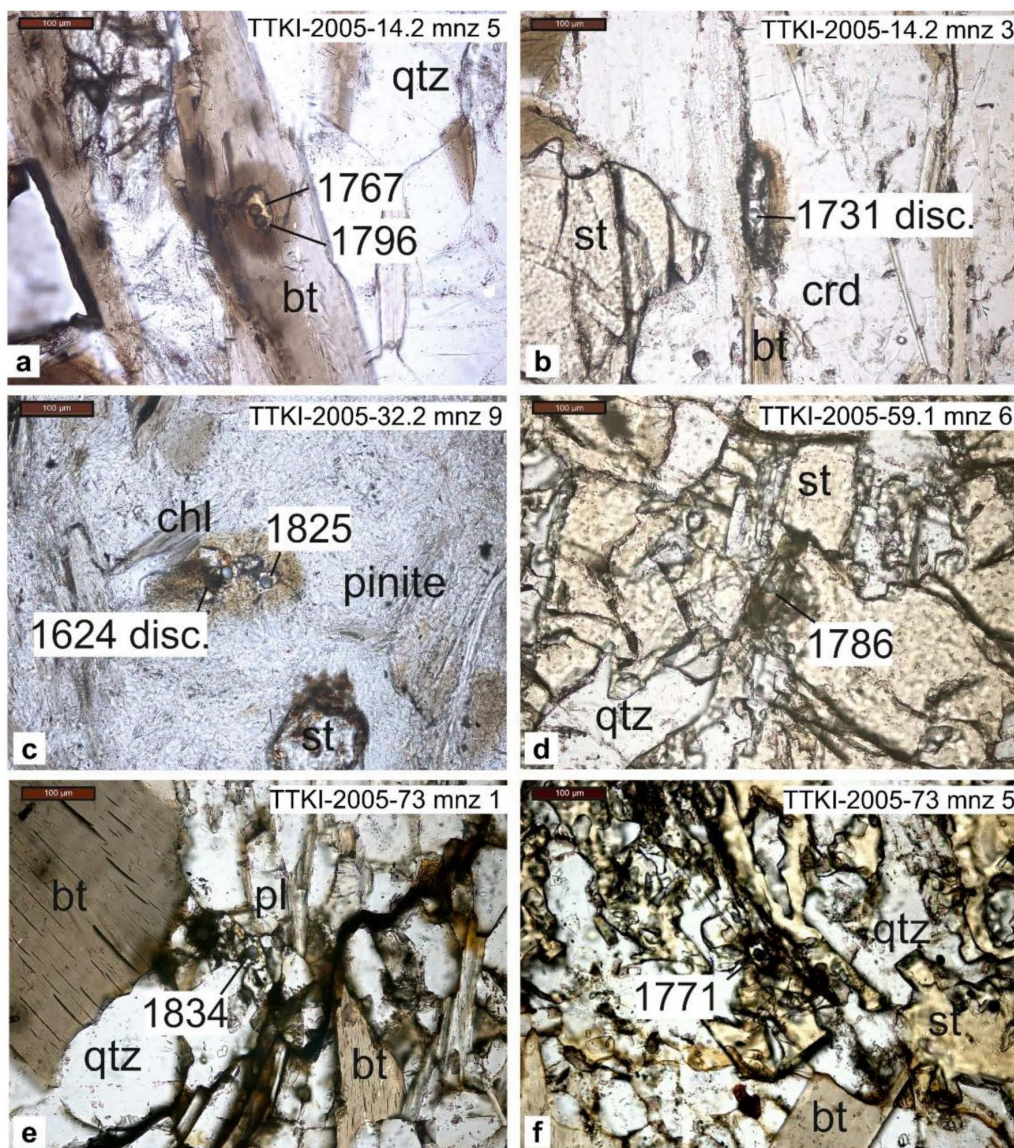


Figure 11. Microphotographs (parallel nicols) of the dated monazite grains showing the $^{207}\text{Pb}/^{206}\text{Pb}$ ages (Ma) for each spot (Supplementary Materials, Table S6). The 2σ error in each age is ± 20 Ma. The scale bar in the upper left corner of each figure is 100 μm . (a) TTKI-2005-14.2, mnz6a and mnz6b; (b) TTKI-2005-14.2, mnz3; (c) TTKI-2005-32.2, mnz9; (d) TTKI-2005-59.1, mnz6; (e) TTKI-2005-73, mnz1; (f) TTKI-2005-73, mnz5.

5.4. Sm-Nd

Metasedimentary rocks from the Tuntsa Suite are LREE enriched (Table S6). The T_{DM} model ages are around 2.8 Ga, suggesting largely relatively juvenile source terrains. The metavolcanic gneiss A1847 and the trondhjemitic gneiss A1846 have low REE contents, A1847 has a flat REE pattern and very low $\epsilon_{\text{Nd}}(t)$ (-15.8), whereas A1846 has extremely low REE contents and Sm/Nd and high $\epsilon_{\text{Nd}}(t)$ ($+3.5$). It seems evident that secondary REE fractionation has been involved, probably during the Paleoproterozoic time.

The Sm-Nd garnet-whole rock dating of the sample A2363 gives an age of 1718 ± 86 Ma (2σ). The $^{147}\text{Sm}/^{144}\text{Nd}$ of garnet in this sample is 0.67 that is rather low (Table S6). The age is quite young but still, within the high error limits, similar to the monazite ages.

5.5. Mineral Equilibria Modelling

Garnet compositions and mineral reactions based on textural observations show considerable changes in PT conditions during the garnet growth. In Figure 12 there are pseudosections for four selected samples (TTKI-2005-14.2, TTKI-2005-32.2, TTKI-2005-59.1, TTKI-2005-73). In these samples, the two textural and compositional types of garnet are represented, as illustrated in Figures 5–7 and Supplementary Materials, Figure S4. Pseudosections are sensitive to the whole rock composition and in many cases it is difficult to establish an effective bulk composition during the garnet growth. For the pseudosection for the samples TTKI-2005-14.2 the used composition was calculated from the modal mineralogy and mineral compositions of the subarea 1 in the thin section (Figure 6, Figure S4). Also for the sample TTKI-2005-32.2, the bulk composition was calculated from a subarea in thin section (Figure S4, Table 1). For the sample TTKI-2005-59.1, the bulk composition was the XRF analyses of the thin section cut-off. For the sample TTKI-2005-73, the XRF analysis of a fist-sized hand specimen was used in the pseudosection because the XRF analysis of the thin section cut-off presumably does not represent the effective bulk composition, large garnet and staurolite porphyroblasts in the small sample overestimating the effective Fe/Mg ratio.

In the sample TTKI-2005-14.2, the pseudosection constructed using the subarea composition did not differ much from that constructed using the composition of the thin section cut-off. The pseudosections were calculated with excess H₂O, assuming that in subsolidus PT conditions dehydration reactions release enough H₂O to keep the system water-saturated. Given the QEMSCAN imaging showed only minor abundances of minerals that could include some ferric iron and the garnet stoichiometry did not indicate it either, Fe₂O₃ was ignored. Small abundances of ferric iron in the whole rock samples would not have much effect in the calculated pseudosections in any case.

Table 1. Whole-rock compositions (mol. %) used for the construction of the pseudosections in Figure 13 and Supplementary Materials, Figure S8. TTKI-2005-14.2 and TTKI-2005-32.2 are calculated from the QEMSCAN modal analyses and mineral compositions, TTKI-2005-59 and TTKI-2005-73 are from XRF analyses. Subarea 1 refers to the area in the thin section presented in Figure 6 and Figure S4 in Supplementary Materials.

	TTKI-2005-14.2	TTKI-2005-59	TTKI-2005-73	TTKI-2005-32.2
	subarea 1			
SiO ₂	55.53	66.17	68.75	47.72
iO ₂	0.76	0.72	0.61	0.75
Al ₂ O ₃	14.84	11.91	11.18	14.40
FeO	7.96	7.16	6.45	9.30
MnO	0.43	0.14	0.07	0.23
MgO	6.35	7.28	6.60	7.47
CaO	2.63	1.81	2.05	0.40
Na ₂ O	3.29	2.68	2.88	0.71
K ₂ O	0.86	2.12	1.40	4.85
H ₂ O(calc.)	7.35			14.18

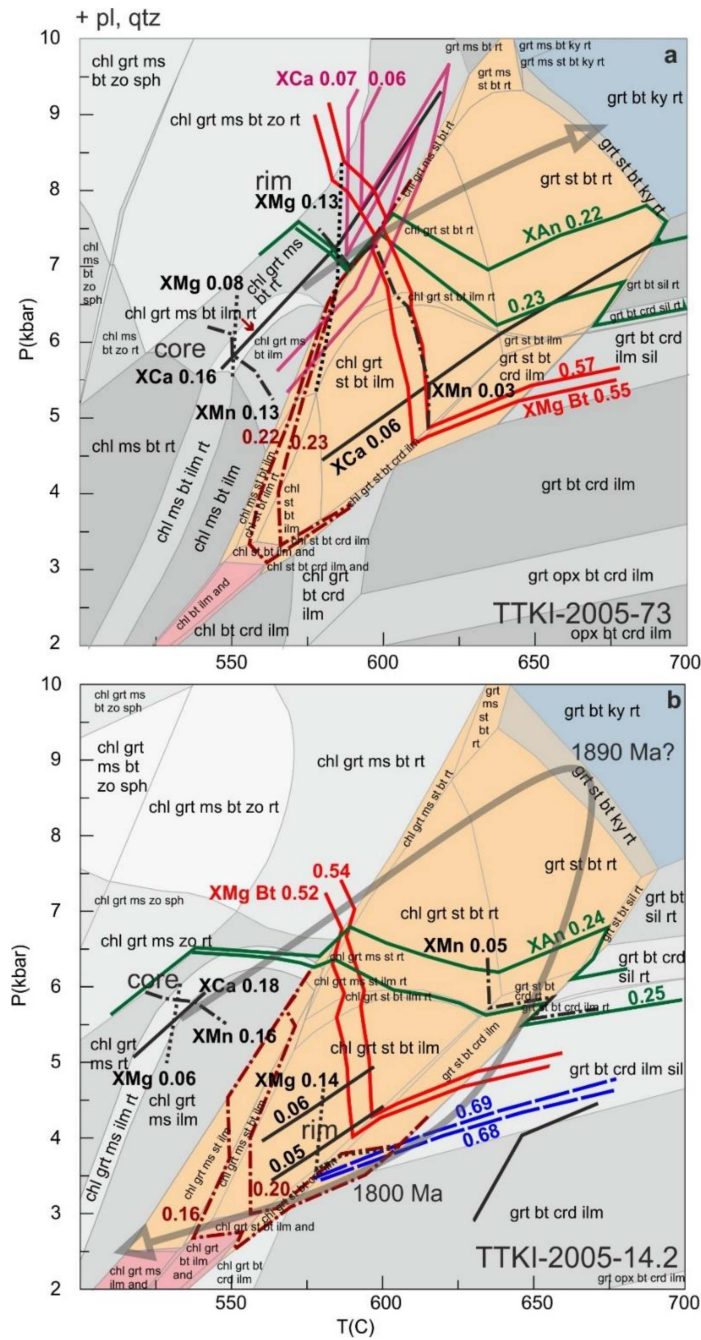


Figure 12. PT pseudosections for the samples TTKI-2005-73 (a) and TTKI-2005-14.2 (b). For clarity, some of the smallest fields for mineral assemblages are left out. The figure also shows the X_{Mg} (dashed), X_{Mn} (dash-dot) and X_{Ca} (solid black lines) isopleths of the analysed garnet cores and rims, and the X_{Mg} and X_{Ca} isopleths for biotite (red lines) and plagioclase (green lines), respectively, and the X_{Mg} isopleths of cordierite in the sample TTKI-2005-14.2 (dashed blue lines). The areas with brownish shades show the stability fields of staurolite, those with bluish shades show the fields for kyanite assemblages and those with pink shades show the fields of andalusite. The grey arrow in Figure 12b TTKI-2005-14.2 displays the possible Proterozoic PT path of the Tuntsa Suite.

6. Discussion and Conclusions

6.1. PT Path

The observed textural and structural features, as well as garnet zoning and isotopic data strongly suggest multiple metamorphisms for the Tuntsa Suite. The first high-grade event was Neoproterozoic, indicated by zircon ages and migmatization (Figure 3c,d). The presence of migmatites, however, is not in accordance either with the present garnet compositions or with the abundance of staurolite in the metasedimentary gneisses. The latter two represent PT conditions where partial melting should not take place, otherwise staurolite would be expected to be found in these whole-rock compositions only as relics, if at all. Both garnet core and rim compositions indicate that the grains were crystallized at subsolidus temperatures, below 700 °C. Also, the kyanite-staurolite assemblages indicate subsolidus metamorphic temperatures in the analyzed whole-rock compositions (Figure 12). Therefore the crystallization of garnet-, staurolite- and kyanite-bearing assemblages must represent another metamorphic cycle, succeeding migmatization.

Figure 12 and Supplementary Materials, Figure S8 display the isopleths for X_{Mg} , X_{Mn} and X_{Ca} within the range of the analyzed garnet grains. If all compositional isopleths for an analyzed area in garnet intersect within errors in a small PT field, then there should be an equilibrium between the garnet and the whole rock within the constraints of the error in the thermodynamic data [85]. For the core compositions the X_{Mg} , X_{Mn} and X_{Ca} isopleths intersect in most cases reasonably well, showing that the crystallization of garnet cores with a high Ca and Mn and low Mg (Figure 7) took place at pressures and temperatures of 5.5–6 kbars and 530–550 °C. This fits well with the observed ilmenite, biotite and muscovite inclusions in garnet. In the QEMSCAN analyses, rutile was found in small abundances in all thin sections. Although rutile inclusions were not detected in garnet, rutile may have been present during the crystallization of early garnet, so that the early paragenesis was Grt-Bt-Chl-Ms-Pl-Qtz-Ilm-Rt which also fits with the P and T mentioned above (Figure 12). The observed composition isopleths of biotite (X_{Mg}) and plagioclase (X_{Ca}) do not fit with the core compositions of garnet and not always with the rim composition either (Figure 12, Figure S8). This indicates disequilibrium, and consequently the uselessness of conventional thermobarometry to estimate PT conditions for the growth of garnet core.

After this, the pressure and temperature must have increased to 7.5–9.5 kbars and c. 640–690 °C where the St-Ky-Bt-Pl-Qtz±Grt±Chl assemblage is stable (Figure 12). Garnet inclusions in some staurolite grains suggest that staurolite was at least in these cases produced by the dehydration reaction $Grt+Chl+Ms = St+Bt+H_2O$. Many garnet grains are zoned, the X_{Mg} increasing to rims which indicates an increasing temperature. However, using pseudosections the PT conditions for the rims are difficult to estimate because of the problems in defining the effective bulk composition. Evans [85] pointed out that the effective bulk composition that should be used in a pseudosection for estimating the PT conditions for the garnet rim is not necessarily the same as the analyzed whole-rock composition because of fractionation of elements in the growing porphyroblasts. Kelsey and Hand [86] argued that in homogenous rocks the bulk compositions could be appropriate for characterizing also the retrograde path, but also noticing that slowly diffusing components in the interiors of large grains become isolated from the reactive rock.

For the garnet rim compositions, the X_{Mn} isopleths in all samples deviate from the intersection point of the X_{Mg} and X_{Ca} isopleths which may reflect the fact that the used bulk composition was not the effective one. Because of the low X_{Mn} in the rim, also the activity-composition relationships for the spessartine component are possibly not correct. Decreasing Ca and increasing Mg suggest that the garnet rim was crystallized in lower pressure and higher temperature than the core, provided that the effective bulk composition did not change much. However, if a lot of Ca was sequestered in the garnet and plagioclase cores, much less Ca was available during the late garnet growth and the interpretation of the Ca zoning becomes different. Garnet in the kyanite-bearing sample TTKI-2005-73 shows strongly decreasing Ca in the rims although there are not any textures indicating decompression. This can be explained by the fact that the abundance of available Ca was very low during the rim growth in which

case the calculated X_{Ca} isopleths have steep dP/dT slopes and the low Ca rims indicate increasing T without decompression. This is illustrated in Figure 12a where the red lines are the X_{Ca} isopleths calculated with the whole rock CaO (mol. %) of 0.35, without changing the abundances of other components. This fits better with the microtexture and assemblage in the thin section, suggesting that the whole garnet crystallized before the D3 crenulation, staurolite and kyanite crystallizing later with increasing T and P during the D3 (Figure S4 and Figure 12a).

Also in the sample TTKI-2005-32.2, the weakly zoned large garnet grains with a low Ca (X_{Ca} 0.05–0.07) and relatively high Mg (X_{Mg} 0.13–0.18 from rim to core) (Supplementary Materials Figures S4 and S8) indicate pressures and temperatures of around 4.5–6 kbars and 570–600 °C if the bulk composition of the thin section cut-off was used in the pseudosection (a test, not shown in the figures). However, the rock is banded in the thin section scale, with plagioclase-rich and garnet-staurolite-biotite rich layers, so that most Ca and Na is concentrated in the plagioclase-rich bands. Therefore the effective bulk composition that determines the garnet composition is that of the layer where garnet is crystallized. The pseudosection in Figure S8 was constructed using the calculated composition in an area delineated in the thin section (Figure S4). Staurolite is strongly sericitized so that at least the K content was changed during retrogression, but anyhow in this low-Ca bulk composition, the calculated X_{Ca} isopleths indicate that garnet core could have crystallized at 7.5–8.5 kbars and 630–660 °C. This is close to the PT conditions where staurolite and kyanite coexist although this sample did not contain kyanite.

Decompression reactions characterize the post-peak metamorphism. Cordierite was produced in the breakdown of staurolite in a reaction such as $St + Chl + Qtz = Crd + Grt + H_2O$ (Figure 5d). In Mg-rich kyanite-bearing rocks cordierite coronas between kyanite and biotite (Figure 5g) were formed in the reaction $Bt + Ky + H_2O = Crd (+ K^+)$. Garnet decomposed locally into cordierite. Rare sillimanite was crystallized on cordierite rims (Figure 5e), suggesting that temperature did not decrease much from that of the peak conditions at this stage.

In the sample TTKI-2005-14.2 (Figures 6 and 7) garnet shows a strong Ca decrease in the rims but the reason for this differs from the previous case. In this sample the straight inclusion trails in the garnet core are truncated at the low-Ca rim, garnet growing clearly during two separate deformation events. The composition of the garnet core (X_{Mg} 0.06, X_{Ca} 0.18) suggests crystallization at 5.5–6 kbars and 530–540 °C. Decomposition of staurolite into cordierite in this sample indicates decompression, as do the low-Ca garnet rim compositions, although the effective bulk composition during the rim growth is difficult to estimate. If the bulk composition is kept the same in the calculation, the intersection of cordierite X_{Mg} (0.68–0.69) and garnet X_{Mg} (c. 0.14) and X_{Ca} (c. 0.05) isopleths suggest crystallization at around 3.5 kbars and 580 °C (Figure 12b).

6.2. Age Determination Methods

The theoretical background and recent advances in zircon, monazite and garnet petrochronology are outside the scope of this paper but the reader is referred to Taylor et al. [87] and papers in Kohn et al. [88]. In metasedimentary rocks, zircon is expected to be mostly detrital in origin, but zircon is also easily crystallized during metamorphism by growth from fluids and, in the case of migmatites, from crystallizing neosome melts [89,90]. There have been several attempts to distinguish metamorphic zircon from igneous one based on morphology, internal zoning, texture and trace element contents [90–92]. It has been observed that the Th/U ratio of metamorphic zircon is generally <0.1 but it may be higher especially in ultra-high temperature rocks lacking other Th-bearing phases; on the other hand, the Th/U ratio of most magmatic zircons is >0.1 [90,93,94].

Monazite is useful for dating metamorphic events because it is easily produced and consumed in solid-state metamorphic reactions. The closure temperature of the U-Pb system in monazite is high, generally considered to be above 700 °C [95]. However, monazite is sensitive to PT changes and fluid flux and composition so that grains in a single specimen can represent either prograde or retrograde stage or both [96–107]. The closure temperature of the U-Pb diffusion is high but monazite

is easily dissolved and reprecipitated during metamorphism, which is likely to be a more efficient mechanism than diffusion for the alteration of the U-Pb system in monazite [95,102,105,106,108,109]. The composition of monazite can be modified in a fluid-related coupled dissolution–reprecipitation process well below the closure temperature of the U-Pb diffusion, even at 450 MPa and 450 °C as experimentally shown by Williams et al. [110].

Garnet dating with Sm-Nd or Lu-Hf isochrons has great potential to unravel metamorphic events. Because of the small abundances of these elements in garnet, modern microbeam methods cannot be used for isotope measurements. Instead, low concentrations can be measured using the TIMS. Pollington and Baxter [111,112] showed that developed cleansing and TIMS techniques can yield accurate and precise Sm-Nd ages on garnet. The isochron slope precision and accuracy depend for example on analytical capacities to measure the parent/daughter isotope ratios and on the purity and elemental zoning of the analysed samples. The retention of microinclusions such as Nd-rich monazite in the garnet separate can affect the age accuracy. If the analysis is made from a bulk multigrain sample where the garnet is age zoned or the rock has several garnet generations, the dates fall somewhere within the garnet growth interval [113,114].

6.3. Ages in Tuntsa

The deposition age of the Tuntsa metasedimentary rocks is problematic. If the trondhjemitic gneiss A1846 represents intrusion at 2.75 Ga into the sediments where the youngest detrital zircon grains yielded by the SIMS analyses are c. 2.77 Ga, then the sedimentation of the Tuntsa Suite was not much older than 2.75 Ga. However, at least some of the contacts between TTGs and metasedimentary gneisses are tectonic (Figure 3a), and if also the trondhjemitic gneiss A1846 has tectonic contacts, the 2.75 Ga age does not constraint the age of sedimentation.

Based on age determinations on metamorphic zircon in granulites and migmatite neosomes, high-grade metamorphism and partial melting occurred at 2.71–2.63 Ga everywhere in the Karelia and Belomorian Provinces. This is also recorded by the abundance of granite-granodiorite-monzogranite intrusions of that age [20,44,115–119]. Therefore it is likely that in high-grade metamorphic rocks, zircon of that age is metamorphic, whatever its composition and textures may be.

In the sample A1843, most zircons whose Th/U is <0.1 are younger than 2.70 Ga, the $^{207}\text{Pb}/^{206}\text{Pb}$ ages of concordant grains being 2.70–2.60 Ga. All zircons that are older than 2.70 Ga have Th/U ratios of >0.2 but there are also a few concordant grains with a Th/U ratio of >0.1 but whose $^{207}\text{Pb}/^{206}\text{Pb}$ age is <2.70 Ga (Figure 8). This could be explained by the Pb loss during the c. 1.80 Ga metamorphism which has changed the isotopic age but not the Th/U ratio. Although the zircon morphology (Supplementary Materials, Figure S5) is ambiguous it is reasonable to conclude that the <2.70 Ga zircons are metamorphic, either originating from high-grade metamorphic sources or representing high-grade metamorphism at 2.70–2.60 Ga. The latter explanation is more plausible. The remnants of migmatitisation (Figure 3c,d) in the Tuntsa Suite could be related with this Neoproterozoic metamorphism as elsewhere in the Archean terrain.

In any case, the Tuntsa Suite underwent strong metamorphism at around 1.80 Ga (Figure 10) which is not so prominent in the juxtaposed complexes. Titanite from syenite in the Tulppio Suite yielded a minimum age of 2.68 Ga and titanite from a granitic gneiss in the Nuruska Complex was dated at 2.65 Ga [59], which support metamorphism also in the Tuntsa Suite at the same time. The preservation of Archean titanites in the juxtaposed granitoid areas is presumably related with the penetrative Proterozoic deformation that was partitioned in the incompetent metasedimentary rocks, activating metamorphic reactions there but leaving the surrounding granitoids largely unaffected. However, based on the existing data, it cannot be completely ruled out that the deposition of the sediments in the Tuntsa Suite took place in the Paleoproterozoic which would also explain the observed differences in titanite and monazite ages.

All monazites from metasedimentary gneisses yielded 1.80–1.79 Ga ages, as well as the leucosome sample A1844 that presumably did not record the time of melting but the Proterozoic metamorphism.

The dated monazites were mostly at grain boundaries and could have crystallized during the late stages of the Paleoproterozoic metamorphism, related with pervasive fluid flow. This is also the case for most monazite dated from Proterozoic metamorphic rocks in the northern Karelia Province [51,84]. However, those monazite grains that are inclusions in biotite and staurolite provided the same 1.80–1.79 Ga age as the other grains (Figure 11). Unfortunately, monazite was not found as inclusions in garnet. Biotite was mostly crystallized during the penetrative D2 deformation and, probably, monazite inclusions crystallized simultaneously with the biotite host.

The Sm-Nd analysis provided large uncertainties in age (1.72 ± 0.9 Ga). Because garnet is zoned in the analyzed sample (Figure S4) there may also be a considerable age difference between the core and the rim. Possibly garnet also had microinclusions with parent/daughter isotope ratios differing from that of the host rock and resulting in erroneously young ages [114]. In any case, the analytical data show that garnet is Paleoproterozoic, not Archean.

6.4. Tectonic Implications

In the northern Fennoscandian Shield collisional and subsequent igneous and exhumation processes between 1.92–1.77 Ga strongly reworked both the Archean bedrock and overlying Paleoproterozoic cover [50,51,56,120–122], leading to similar metamorphic and structural style regardless of age. Gently dipping nappe and overthrust structures, like those in Tuntsa (Figure 3a,b), are common also in juxtaposed Proterozoic formations [123,124]. Kyanite is commonly found in the Proterozoic metasedimentary rocks west of the Tuntsa Suite (Figure 1) [124–126] and similar clockwise cooling paths as in Tuntsa have been described from the Proterozoic rocks in Central Lapland and the Lapland Granulite Complex and its southern contact zone [121,124,127].

U-Pb data on metamorphic zircon from eclogites and cross-cutting pegmatites in Kuru-Vaara, c. 100 km east of Tuntsa suggests high-pressure metamorphism in the northern Belomorian Province at 1.90–1.89 Ga [38]. In the Kovdozero-Tolstik area c. 150 km southeast of Tuntsa, Skiöld et al. [13] found in the Archean rocks metamorphic zircons of 1875 Ma and titanites of 1860 Ma. They related those ages with the peak Proterozoic metamorphism at around 650 °C and 9 kbar and subsequent cooling during the Lapland-Kola continental collision. U-Pb ages on rutile in that area were 1780–1740 Ma, as elsewhere in the Belomorian Province [10]. These ages were interpreted to represent cooling down to c. 400 °C [13]. Corfu and Evins [4] reported 1.78–1.77 Ga U-Pb ages on titanite and monazite in the nearby Archean Suomujärvi complex (Figure 1), arguing that the crystallization of these minerals was coeval with the development of metamorphic fabric and regional deformation.

According to tectonic models by Daly et al. [16] and Lahtinen et al. [51,120] for the Lapland-Kola and Svecofennia orogens, thrusting both from the present SE and from the NE at 1.92–1.91 Ga thickened the crust tectonically. Lahtinen and Huhma [9] recently proposed a model where the Lapland-Kola Province collided with the Karelia Province at 1.92–1.91 Ga (Figure 13). Large thrust nappes formed on the foreland and the lower plate subducted leading locally to eclogite facies metamorphism. Another compressional event at 1.88–1.87 Ga caused the present duplex structure of the Lapland Granulite Complex and uplift of granulites and eclogites. After that, there was a large-scale orocline formation that caused the present arc-like structure of the Complex. The final cooling of the Lapland-Kola orogen took place at 1.79–1.76 Ga, marked by the emplacement of post-tectonic granites.

Lapland granulites, originally metamorphosed at 750–850 °C and 5–9 kbars at c. 1.91 Ga were uplifted to 2–3 kbars at 1.88 Ga. This interpretation was based on the existence of large euhedral andalusite grains in textural equilibrium with feldspar and quartz in migmatite leucosomes giving zircon ages of 1.88 Ga. Paleosomes of the same migmatites yielded c. 1.91 Ga U-Pb ages on metamorphic zircon and monazite [121,122]. However, the zircon age does not necessarily date the andalusite crystallization, especially because both leucosomes and paleosomes of the migmatitic granulites also have yielded 1.89–1.88 Ga garnet-whole rock Sm-Nd ages in an area where garnet-based geobarometry has yielded pressures of 6–8 kbars [121,128], suggesting that at that time the granulites still were at relatively high pressures. Hölttä et al. [84] dated garnet from two paragneiss exposures c. 20–30 km

south of the Lapland Granulite Complex (LGC), 80–100 km NW of Tuntsa, yielding Sm-Nd garnet-whole rock ages of 1.85–1.84 Ga, one of the two with relatively small 2σ error limits (1843 ± 12 Ma, Table S3 in Hölttä et al. [84]). In this area, maximum metamorphic temperatures were 600–700 °C at pressures of 7–10 kbars [124], therefore the Sm-Nd ages presumably are close to garnet crystallization ages. In our samples, a few monazite grains yielded 1.84–1.83 Ga ages which could indicate that also in Tuntsa the peak PT conditions were achieved at around 1.84 Ga.

Figure 13 presents a cartoon of the tectonic evolution of the Tuntsa Suite and adjacent areas. In this scenario, the granulites were exhumed after 1.89 Ga when thrust onto the adjacent Archean and Proterozoic that were buried and heated at medium pressures between 1.89–1.84 Ga. The penetrative subhorizontal D2 foliation (Figure 3a,b) presumably developed at this stage. The uplift of the rocks south of the LGC would have started soon after that while the crust was still hot, monazite crystallizing after that continuously until final cooling and cratonization of the crust at 1.77–1.76 Ga.

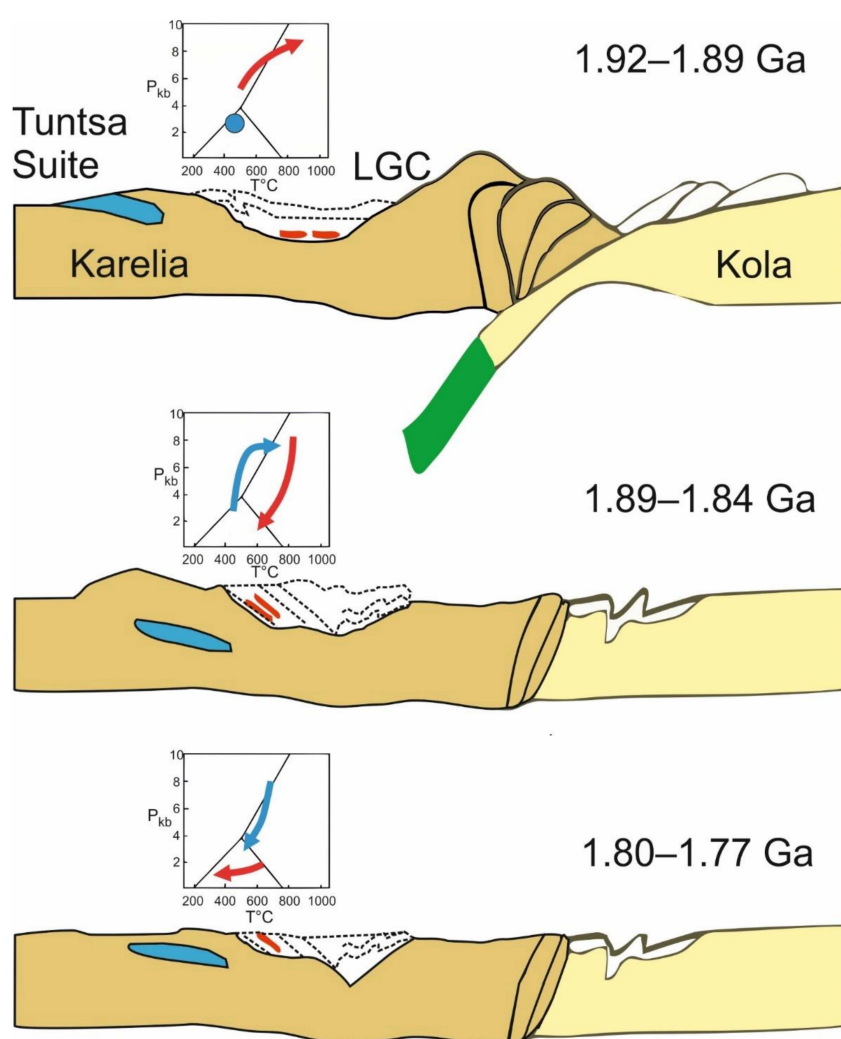


Figure 13. A cartoon illustrating the tectonic development of the Tuntsa suite as a function of time, modified from Lahtinen and Huhma [9]. LGC = Lapland Granulite Complex. The blue dot and arrow in the PT diagram illustrate the PT path of the Tuntsa Suite and the red arrow that of the LGC.

7. Conclusions

- The Tuntsa Suite is a polymetamorphic Precambrian complex consisting mostly of metasedimentary rocks whose deposition took place in the early Neoproterozoic. It was metamorphosed twice, first at high grade around 2.70–2.64 Ga, related with the assembly of the Kenorland supercontinent. The second metamorphic cycle took place at 1.84–1.79 Ga when the Suite underwent a penetrative deformation and medium grade Barrovian style metamorphism, producing a clockwise PT path as a result of crustal thickening and subsequent exhumation.
- The Proterozoic metamorphism was caused by the thrusting of the Lapland granulites onto the adjacent areas. All metamorphic mineral assemblages, including monazite, are Proterozoic, the remnants of migmatites and metamorphic zircon witnessing the Archean metamorphism.
- Monazite and garnet record only the Proterozoic metamorphism.
- The Proterozoic pressure-temperature development is seen in garnet zoning, but the commonly observed zoning where Mg increases and Ca decreases from the core to the rim can develop with both increasing and decreasing pressure, depending on the effective bulk composition and Ca sequestering in early metamorphic minerals.

Supplementary Materials: The following are available online at <http://www.mdpi.com/2075-163X/10/11/1034/s1>, Table S1. List of all samples and their mineral associations studied in this work. Table S2. Selected microprobe analyses. Table S3. Results of the QEMSCAN analyses. Figure S4. QEMSCAN images. Figure S5. Back-scattered electrons images of zircon grains dated using the Nordsim ion microprobe. The numbers refer to the analysis spots and $^{207}\text{Pb}/^{206}\text{Pb}$ ages presented in Table S6. Table S6. Isotopic analytical data. Supplementary Materials S7. Petrography of the imaged and PT modelled samples. Figure S8. PT pseudosections for the samples TTKI-2005-59 and TTKI-2005-32.2.

Author Contributions: Conceptualization, P.H.; Methodology, P.H., H.H., M.K., G.R. and A.R.B.; Software, P.H., H.H., M.K., G.R.; Validation, P.H., H.H., M.K. and G.R.; Formal Analysis, P.H., T.K., H.H., G.R. and A.R.B.; Investigation, P.H. and T.K.; Resources, P.H.; Data Curation, P.H.; Writing—Original Draft Preparation, P.H., T.K., H.H., G.R.; Writing—Review & Editing, P.H., H.H., M.K., G.R. and A.R.B.; Visualization, P.H., T.K., H.H., M.K., G.R. and A.R.B.; Supervision, P.H.; Project Administration, P.H. All authors have read and agreed to the published version of the manuscript.

Funding: This research received no external funding.

Acknowledgments: Lassi Pakkanen is thanked for the microprobe analytics and Sari Lukkari for the SEM analyses. Tom Andersen, Yann Lahaye, Hugh O'Brien, Tuula Hokkanen, Leena Järvinen and Arto Pulkkinen are gratefully acknowledged for the help in the isotope analyses at the GTK, Martin Whitehouse for the help with the NORDSIM. Geological Survey of Finland is acknowledged for the funding of the NORDSIM work. The constructive comments of the anonymous reviewers and MDPI editors are gratefully acknowledged.

Conflicts of Interest: The authors declare no conflict of interest.

References

1. Pajunen, M.; Poutiainen, M. Palaeoproterozoic prograde metasomatic-metamorphic overprint zones in Archean tonalitic gneisses, eastern Finland. *Bull. Geol. Soc. Finl.* **1999**, *71*, 73–132. [[CrossRef](#)]
2. Mänttari, I.; Hölttä, P. U-Pb dating of zircons and monazites from Archean granulites in Varpaisjärvi, central Finland: Evidence for multiple metamorphism and Neoproterozoic terrane accretion. *Precambrian Res.* **2002**, *118*, 101–131.
3. Hölttä, P.; Lehtonen, E.; Lahaye, J.; Sorjonen-Ward, P. Metamorphic evolution of the Ilomantsi greenstone belt in the Archean Karelia Province, eastern Finland. *Geol. Soc. Lond. Spec. Publ.* **2017**, *449*, 231–250. [[CrossRef](#)]
4. Corfu, F.; Evins, P.M. Late Palaeoproterozoic monazite and titanite U–Pb ages in the Archean Suomijärvi Complex, N-Finland. *Precambrian Res.* **2002**, *116*, 171–181. [[CrossRef](#)]
5. Huhma, H.; Hanski, E.; Kontinen, A.; Vuollo, J.; Mänttari, I.; Lahaye, Y. Sm–Nd and U–Pb isotope geochemistry of the Palaeoproterozoic mafic magmatism in eastern and northern Finland. *Bull. Geol. Soc. Finl.* **2018**, *405*, 1–150.
6. Larionova, Y.O.; Samsonov, A.V.; Shatagin, K.N.; Nosova, A.A. Isotopic Geochronological Evidence for the Paleoproterozoic Age of Gold Mineralization in Archean Greenstone Belts of Karelia, the Baltic Shield. *Geol. Ore Depos.* **2013**, *55*, 320–340. [[CrossRef](#)]

7. Kontinen, A.; Paavola, J.; Lukkarinen, H. K-Ar ages of hornblende and biotite from late Archaean rocks of eastern Finland; interpretation and discussion of tectonic implications. *Bull. Geol. Soc. Finl.* **1992**, *365*, 5–31.
8. Mertanen, S.; Halls, H.C.; Vuollo, J.I.; Pesonen, L.J.; Stepanov, V.S. Paleomagnetism of 2.44 Ga mafic dykes in Russian Karelia, eastern Fennoscandian Shield; implications for continental reconstructions. *Precambrian Res.* **1999**, *98*, 197–221. [[CrossRef](#)]
9. Lahtinen, R.; Huhma, H. A revised geodynamic model for the Lapland-Kola orogen. *Precambrian Res.* **2019**, *330*, 1–19. [[CrossRef](#)]
10. Bibikova, E.; Skiöld, T.; Bogdanova, S.; Gorbatshev, R.; Slabunov, A. Titanite-rutile thermochronometry across the boundary between the Archaean Craton in Karelia and the Belomorian Mobile Belt, eastern Baltic Shield. *Precambrian Res.* **2001**, *105*, 315–330. [[CrossRef](#)]
11. Balagansky, V.; Shchipansky, A.; Slabunov, A.I.; Gorbunov, I.; Mudruk, S.; Sidorov, M.; Azimov, P.; Egorova, S.; Stepanov, A.; Voloshin, A. Archaean Kuru-Vaara eclogites in the northern Belomorian Province, Fennoscandian Shield: Crustal architecture, timing, and tectonic implications. *Int. Geol. Rev.* **2015**, *57*, 1543–1565. [[CrossRef](#)]
12. Dokukina, K.A.; Kaulina, T.V.; Konilov, A.N.; Mints, M.V.; Van, K.V.; Natapov, L.; Belousova, E.; Simakin, S.G.; Lepekhina, E.N. Archaean to Palaeoproterozoic high-grade evolution of the Belomorian eclogite province in the Gridino area, Fennoscandian Shield: Geochronological evidence. *Gondwana Res.* **2014**, *25*, 585–613. [[CrossRef](#)]
13. Skiöld, T.; Bogdanova, S.; Gorbatshev, R.; Bibikova, E. Timing of late Palaeoproterozoic metamorphism in the northern Belomorian Belt, White Sea region; conclusions from U-Pb isotopic data and P-T evidence. *Bull. Geol. Soc. Finl.* **2001**, *73*, 59–73. [[CrossRef](#)]
14. Gaál, G. 2200 million years of crustal evolution: The Baltic Shield. *Bull. Geol. Soc. Finl.* **1986**, *58*, 149–168. [[CrossRef](#)]
15. Gaál, G.; Gorbatshev, R. An Outline of the Precambrian Evolution of the Baltic Shield. *Precambrian Res.* **1987**, *35*, 15–52. [[CrossRef](#)]
16. Daly, J.S.; Balagansky, V.V.; Timmerman, M.J.; Whitehouse, M.J. The Lapland-Kola orogen: Palaeoproterozoic collision and accretion of the northern Fennoscandian lithosphere. *Geol. Soc. Mem.* **2006**, *32*, 579–598. [[CrossRef](#)]
17. Nironen, M. Guide to the Geological Map of Finland – Bedrock 1:1 000 000. *Spec. Pap. Geol. Surv. Finl.* **2017**, *60*, 40–74.
18. Hölttä, P.; Balagansky, V.; Garde, A.A.; Mertanen, S.; Peltonen, P.; Slabunov, A.; Sorjonen-Ward, P.; Whitehouse, M. Archean of Greenland and Fennoscandia. *Episodes* **2008**, *31*, 13–19. [[CrossRef](#)]
19. Hölttä, P.; Heilimo, E.; Huhma, H.; Kontinen, A.; Mertanen, S.; Mikkola, P.; Paavola, J.; Peltonen, P.; Semprich, J.; Slabunov, A.; et al. The Archaean Karelia and Belomorian Provinces, Fennoscandian Shield. In *Evolution of Archean Crust and Early Life*; Dilek, Y., Furnes, H., Eds.; Springer: Berlin, Germany, 2014; Volume 7, pp. 55–102.
20. Hölttä, P.; Heilimo, E.; Huhma, H.; Kontinen, A.; Mertanen, S.; Mikkola, P.; Paavola, J.; Peltonen, P.; Semprich, J.; Slabunov, A.; et al. The Archaean of the Karelia Province in Finland. *Spec. Pap. Geol. Surv. Finl.* **2012**, *2012*, 21–73.
21. Volodichev, O.I. *Metamorphism of Kyanite Facies Gneisses (Example from the Belomorian Complex)*; Nauka: Leningrad, FL, USA, 1975; p. 170.
22. Volodichev, O.I. *The Belomorian Complex of Karelia: Geology and Petrology*; Nauka: Leningrad, FL, USA, 1990; p. 248.
23. Shchipansky, A.A.; Babarina, I.I.; Krylov, K.A.; Samsonov, A.V.; Bogina, M.M.; Bibikova, E.V.; Slabunov, A.I. The oldest ophiolites: The late Archean suprasubduction zone complex of the Iringora structure, north Karelian greenstone belt. *Dokl. Earth Sci.* **2001**, *377 A*, 283–287.
24. Mints, M.V.; Berzin, R.G.; Andryushchenko, Y.N.; Zamozhnyaya, N.G.; Zlobin, V.L.; Konilov, A.N.; Stupak, V.M.; Suleimanov, A.K. The deep structure of the Karelian Craton along geotraverse 1-EB. *Geotectonics* **2004**, *38*, 329–342.
25. Mints, M.; Berzin, R.G.; Suleimanov (Suleymanov), A.K.; Zamozhnyaya, N.G.; Stupak, V.M.; Konilov, A.N.; Zlobin, V.L.; Kaulina, T.V. The deep structure of the early Precambrian crust of the Karelian Craton, southeastern Fennoscandian Shield; results of investigation along CMP profile 4B. *Geotectonics* **2004**, *38*, 87–102.

26. Sharov, N.V.; Kulikov, V.S.; Kulikova, V.V.; Isanina, E.V.; Krupnova, N.A. Crustal seismogeological characteristics in the southeastern Fennoscandian Shield (Russia). *Geofiz. Zhurnal* **2010**, *32*, 3–17. [[CrossRef](#)]
27. Perchuk, A.L.; Morgunova, A.A. Variable P–T paths and HP–UHP metamorphism in a Precambrian terrane, Gridino, Russia: Petrological evidence and geodynamic implications. *Gondwana Res.* **2014**, *25*, 614–629. [[CrossRef](#)]
28. Volodichev, O.I.; Slabunov, A.I.; Bibikova, E.V.; Konilov, A.N.; Kuzenko, T.I. Archean eclogites in the Belomorian mobile belt, Baltic shield. *Petrology* **2004**, *12*, 540–560.
29. Dokukina, K.A.; Mints, M.V.; Konilov, A.N. Melting of eclogite facies sedimentary rocks in the Belomorian Eclogite Province, Russia. *J. Metamorph. Geol.* **2017**, *35*, 435–451. [[CrossRef](#)]
30. Mints, M.V.; Belousova, E.A.; Konilov, A.N.; Natapov, L.M.; Shchipansky, A.A.; Griffin, W.L.; O'Reilly, S.Y.; Dokukina, K.A.; Kaulina, T.V. Mesoarchean subduction processes: 2.87 Ga eclogites from the Kola Peninsula, Russia. *Geology* **2010**, *38*, 739–742. [[CrossRef](#)]
31. Mints, M.V.; Dokukina, K.A.; Konilov, A.N. The Meso-Neoproterozoic Belomorian eclogite province: Tectonic position and geodynamic evolution. *Gondwana Res.* **2014**, *25*, 561–584. [[CrossRef](#)]
32. Shchipansky, A.A.; Khodorevskaya, L.I.; Konilov, A.N.; Slabunov, A.I. Eclogites from the Belomorian Mobile Belt (Kola Peninsula): Geology and petrology. *Russ Geol Geophys.* **2012**, *53*, 1–21. [[CrossRef](#)]
33. Mints, M.V.; Konilov, A.N.; Dokukina, K.A.; Kaulina, T.V.; Belousova, E.A.; Natapov, L.M.; Griffin, W.L.; O'Reilly, S.Y. The Belomorian eclogite province: Unique evidence of Meso-Neoproterozoic subduction and collision. *Dokl. Earth Sci.* **2010**, *434*, 1311–1316. [[CrossRef](#)]
34. Dokukina, K.A.; Konilov, A.N.; Van, K.V.; Mints, M.V.; Simakin, S.G. Origin of early Paleoproterozoic zircons in rocks of the Archean eclogite association of Gridino (Belomorian eclogite province). *Dokl. Earth Sci.* **2012**, *445*, 832–839. [[CrossRef](#)]
35. Kaulina, T.V.; Yapaskurt, V.O.; Presnyakov, S.L.; Savchenko, E.E.; Simakin, S.G. Metamorphic evolution of the Archean eclogite-like rocks of the Shirokaya and Uzkaya Salma area (Kola Peninsula): Geochemical features of zircon, composition of inclusions, and age. *Geochem. Int.* **2010**, *48*, 871–890. [[CrossRef](#)]
36. Mints, M.V.; Dokukina, K.A. Age of eclogites formed by the subduction of the Mesoarchean oceanic crust (Salma, Belomorian Eclogite Province, eastern Fennoscandian Shield, Russia): A synthesis. *Precambrian Res.* **2020**, *350*, 105879. [[CrossRef](#)]
37. Li, X.; Yu, H.; Zhang, L.; Wei, C.; Bader, T. 1.9 Ga eclogite from the Archean-Paleoproterozoic Belomorian Province, Russia. *Sci. Bull.* **2017**, *62*, 239–241. [[CrossRef](#)]
38. Liu, F.; Zhang, L.; Li, X.; Slabunov, A.I.; Wei, C.; Bader, T. The metamorphic evolution of Paleoproterozoic eclogites in Kuru-Vaara, northern Belomorian Province, Russia: Constraints from P–T pseudosections and zircon dating. *Precambrian Res.* **2017**, *289*, 31–47. [[CrossRef](#)]
39. Yu, H.; Zhang, L.; Lanari, P.; Rubatto, D.; Li, X. Garnet Lu–Hf geochronology and P–T path of the Gridino-type eclogite in the Belomorian Province, Russia. *Lithos* **2019**, *326–327*, 313–326. [[CrossRef](#)]
40. Skublov, S.G.; Balashov, Y.A.; Marin, Y.B.; Berezin, A.V.; Mel'nik, A.E.; Paderin, I.P. U–Pb age and geochemistry of zircons from Salma eclogites (Kuru-Vaara Deposit, Belomorian Belt). *Dokl. Earth Sci.* **2010**, *432*, 791–798. [[CrossRef](#)]
41. Imayama, T.; Oh, C.; Baltybaev, S.K.; Park, C.Y.K.; Jung, H. Paleoproterozoic high-pressure metamorphic history of the Salma eclogite on the Kola Peninsula, Russia. *Lithosphere* **2017**, *9*, 855–873. [[CrossRef](#)]
42. Herwartz, D.; Skublov, S.G.; Berezin, A.V.; Melnik, A.E. First Lu–Hf Garnet Ages of Eclogites from the Belomorian Mobile Belt (Baltic Shield, Russia). *Dokl. Earth Sci.* **2012**, *443*, 377–380. [[CrossRef](#)]
43. Berezin, A.V.; Travin, V.V.; Marin, Y.B.; Skublov, S.G.; Bogomolov, E.S. New U–Pb and Sm–Nd Ages and P–T Estimates for Eclogitization in the Fe-Rich Gabbro Dyke in Gridino Area (Belomorian Mobile Belt). *Dokl. Earth Sci.* **2012**, *444*, 760–765. [[CrossRef](#)]
44. Dokukina, K.A.; Kaulina, T.V.; Konilov, A.N. Dating of key events in the Precambrian polystage complexes: An example from Archean Belomorian Eclogite Province, Russia. *Dokl. Earth Sci.* **2009**, *425*, 296–301. [[CrossRef](#)]
45. Travin, V.V.; Kozlova, N.E. Eclogitization of basites in early proterozoic shear zones in the area of the village of Gridino, western Belomorie. *Petrology* **2009**, *17*, 684–706. [[CrossRef](#)]
46. Hanski, E.J.; Huhma, H.; Rastas, P.; Kamenetsky, V.S. The Palaeoproterozoic Komatiite–Picrite Association of Finnish Lapland. *J. Petrol.* **2001**, *42*, 855–876. [[CrossRef](#)]

47. Hanski, E.; Huhma, H. Central Lapland greenstone belt. In *Precambrian Geology of Finland. Key to the Evolution of the Fennoscandian Shield*; Lehtinen, M., Nurmi, P.A., Rämö, O.T., Eds.; Elsevier: Amsterdam, The Netherlands, 2005; Volume 14, pp. 139–193.
48. Hanski, E.; Melezhik, V.A. Litho- and chronostratigraphy of the Paleoproterozoic Karelian formations. In *Reading the Archive of Earth's Oxygenation, Volume 1: The Palaeoproterozoic of Fennoscandia as Context for the Fennoscandian Arctic Russia—Drilling Early Earth Project*; Melezhik, V.A., Prave, A.R., Fallick, A.E., Kump, L.R., Strauss, H., Lepland, A., Hanski, E.J., Eds.; Springer-Verlag: Berlin, Germany, 2013; pp. 39–110.
49. Köykkä, J.; Lahtinen, R.; Huhma, H. Provenance evolution of the Paleoproterozoic metasedimentary cover sequences in northern Fennoscandia: Age distribution, geochemistry, and zircon morphology. *Precambrian Res.* **2019**, *331*, 105364. [[CrossRef](#)]
50. Lahtinen, R.; Huhma, H.; Lahaye, Y.; Jonsson, E.; Manninen, T.; Lauri, L.S.; Bergman, S.; Hellström, F.; Niiranen, T.; Nironen, M. New geochronological and Sm–Nd constraints across the Pajala shear zone of northern Fennoscandia: Reactivation of a Paleoproterozoic suture. *Precambrian Res.* **2015**, *256*, 102–119. [[CrossRef](#)]
51. Lahtinen, R.; Huhma, H.; Sayab, M.; Lauri, L.S.; Hölttä, P. Age and structural constraints on the tectonic evolution of the Paleoproterozoic Central Lapland Granitoid Complex in the Fennoscandian Shield. *Tectonophysics* **2018**, 305–325. [[CrossRef](#)]
52. Melezhik, V.A.; Hanski, E.J. Palaeotectonic and Palaeogeographic evolution of Fennoscandia in the Palaeoproterozoic. In *Reading the Archive of Earth's Oxygenation. Volume 1: The Palaeoproterozoic of Fennoscandia as Context for the Fennoscandian Arctic Russia—Drilling Early Earth Project*; Melezhik, V.A., Prave, A.R., Fallick, A.E., Kump, L.R., Strauss, H., Lepland, A., Hanski, E.J., Eds.; Springer-Verlag: Berlin, Germany, 2013; pp. 111–178.
53. Peltonen, P.; Mänttari, I.; Huhma, H.; Kontinen, A. Archean zircons from the mantle: The Jormua ophiolite revisited. *Geology* **2003**, *31*, 645–648. [[CrossRef](#)]
54. Peltonen, P.; Kontinen, A.; Huhma, H.; Kuronen, U. Outokumpu revisited: New mineral deposit model for the mantle peridotite-associated Cu–Co–Zn–Ni–Ag–Au sulphide deposits. *Ore Geol. Rev.* **2008**, *33*, 559–617. [[CrossRef](#)]
55. Vuollo, J.; Huhma, H. Paleoproterozoic mafic dikes in NE Finland. In *Precambrian Geology of Finland – Key to the Evolution of the Fennoscandian Shield*; Lehtinen, M., Nurmi, P.A., Rämö, O.T., Eds.; Elsevier B.V.: Amsterdam, The Netherlands, 2005; pp. 195–236.
56. Ahtonen, N.; Hölttä, P.; Huhma, H. Intracratonic Palaeoproterozoic granitoids in northern Finland: Prolonged and episodic crustal melting events revealed by Nd isotopes and U–Pb ages on zircon. *Bull. Geol. Soc. Finl.* **2007**, *79*, 143–174. [[CrossRef](#)]
57. Ranta, J.; Lauri, L.S.; Hanski, E.; Huhma, H.; Lahaye, Y.; Vanhanen, E. U–Pb and Sm–Nd isotopic constraints on the evolution of the Paleoproterozoic Peräpohja Belt, northern Finland. *Precambrian Res.* **2015**, 246–259. [[CrossRef](#)]
58. Juopperi, H. *Kallioperäkarta 1:100,000-Maps of Pre-Quaternary Rocks, Sheets 3733 and 4711, Savukoski*; Geological Survey of Finland: Espoo, Finland, 1986.
59. Juopperi, H.; Vaasjoki, M. U–Pb mineral age determinations from Archean rocks in eastern Lapland. *Spec. Pap. Geol. Surv. Finl.* **2001**, *33*, 209–227.
60. Sawyer, E.W. Working with migmatites: Nomenclature for the constituent parts. In *Working with Migmatites*; Sawyer, E.W., Brown, M., Eds.; Mineralogical Association of Canada: Quebec, QC, Canada, 2008; Volume 38, pp. 1–28.
61. Juopperi, H.; Veki, A. The Archaean Tuntsa Supergroup in the Nuolusvaara area, northeastern Finland. *Spec. Pap. Geol. Surv. Finl.* **1988**, *4*, 145–149.
62. Gottlieb, P.; Wilkie, G.; Sutherland, D.; Ho-Tun, E.; Suthers, S.; Perera, K.; Jenkins, B.; Spencer, S.; Butcher, A.; Rayner, J. Using quantitative electron microscopy for process mineralogy applications. *JOM* **2000**, *52*, 24–25. [[CrossRef](#)]
63. Pirrie, D.; Butcher, A.R.; Power, M.R.; Gottlieb, P.; Miller, G.L. Rapid quantitative mineral and phase analysis using automated scanning electron microscopy (QEMSCAN); potential applications in forensic geoscience. *Geol. Soc. Lond. Spec. Publ.* **2004**, *232*, 123–136. [[CrossRef](#)]
64. Goodall, W.R.; Scales, P.J.; Butcher, A.R. The use of QEMSCAN and diagnostic leaching in the characterisation of visible gold in complex ores. *Miner. Eng.* **2005**, *18*, 877–886. [[CrossRef](#)]

65. Pirrie, D.; Rollinson, G.K. Unlocking the applications of automated mineral analysis. *Geol. Today* **2011**, *27*, 226–235. [[CrossRef](#)]
66. Rollinson, G.K.; Anderson, J.C.Ø.; Stickland, R.J.; Boni, M.; Fairhurst, R. Characterisation of non-sulphide zinc deposits using QEMSCAN. *Miner. Eng.* **2011**, *24*, 778–787. [[CrossRef](#)]
67. Andersen, J.C.Ø.; Rollinson, G.K.; Snook, B.; Herrington, R.; Fairhurst, R.J. Use of QEMSCAN® for the characterization of Ni-rich and Ni-poor goethite in laterite ores. *Miner. Eng.* **2009**, *22*, 1119–1129. [[CrossRef](#)]
68. Huhma, H.; Kontinen, A.; Mikkola, P.; Halkoaho, T.; Hokkanen, T.; Hölttä, P.; Juopperi, H.; Konnunaho, J.; Luukkonen, E.; Mutanen, T.; et al. Nd isotopic evidence for Archaean crustal growth in Finland. *Spec. Pap. Geol. Surv. Finl.* **2012**, *54*, 176–214.
69. Huhma, H.; Mänttari, I.; Peltonen, P.; Kontinen, A.; Halkoaho, T.; Hanski, E.; Hokkanen, T.; Holttä, P.; Juopperi, H.; Konnunaho, J.; et al. The age of the Archaean greenstone belts in Finland. *Spec. Pap. Geol. Surv. Finl.* **2012**, *54*, 74–175.
70. Stacey, J.S.; Kramers, J.D. Approximation of terrestrial lead isotope evolution by a two-stage model. *Earth Planet. Sci. Lett.* **1975**, *26*, 207–221. [[CrossRef](#)]
71. Mattinson, J.M. Zircon U-Pb chemical abrasion ("CA-TIMS") method: Combined annealing and multi-step partial dissolution analysis for improved precision and accuracy of zircon ages. *Chem. Geol.* **2005**, *220*, 47–66. [[CrossRef](#)]
72. Whitehouse, M.J.; Kamber, B.S. Assigning dates on thin gneissic veins in high-grade metamorphic terranes; a cautionary tale from Akilia, southwest Greenland. *J. Petrol.* **2005**, *46*, 291–318. [[CrossRef](#)]
73. Mueller, W.; Shelley, J.M.G.; Rasmussen, S.O. Direct analysis of ice cores by UV-laser ablation ICPMS. *Geochim. Cosmochim. Acta* **2009**, *73*, A915.
74. Rosa, D.R.N.; Finch, A.A.; Andersen, T.; Inverno, C.M.C. U-Pb geochronology and Hf isotope ratios of magmatic zircons from the Iberian pyrite belt. *Mineral. Petrol.* **2009**, *95*, 47–69. [[CrossRef](#)]
75. Van Achterbergh, E.; Ryan, C.; Jackson, S.; Griffin, W. Data reduction software for LA-ICP-MS. In *Laser-Ablation ICPMS in the Earth Sciences—Principles and Applications*; Sylvester, P., Ed.; Mineralogical Association of Canada: Québec, QC, Canada, 2001; Volume 29, pp. 239–243.
76. Ludwig, K.R. User's Manual for Isoplot 3.75. A Geochronological Toolkit for Microsoft Excel. *Berkeley Geochronol. Cent. Spec. Publ.* **2012**, *5*, 1–75.
77. Connolly, J.A.D.; Petrini, K. An automated strategy for calculation of phase diagram sections and retrieval of rock properties as a function of physical conditions. *J. Metamorph. Geol.* **2002**, *20*, 697–708. [[CrossRef](#)]
78. Connolly, J.A.D. The geodynamic equation of state: What and how. *Geochem. Geophys. Geosyst.* **2009**, *10*, 19. [[CrossRef](#)]
79. Holland, T.J.B.; Powell, R. An improved and extended internally consistent thermodynamic dataset for phases of petrological interest, involving a new equation of state for solids. *J. Metamorph. Geol.* **2011**, *29*, 333–383. [[CrossRef](#)]
80. Holland, T.; Powell, R. Activity–composition relations for phases in petrological calculations: An asymmetric multicomponent formulation. *Contrib. Miner. Pet.* **2003**, *145*, 492–501. [[CrossRef](#)]
81. White, R.W.; Powell, R.; Holland, T.J.B.; Johnson, T.E.; Green, E.C.R. New mineral activity–composition relations for thermodynamic calculations in metapelitic systems. *J. Metamorph. Geol.* **2014**, *32*, 261–286. [[CrossRef](#)]
82. Kretz, R. Symbols for rock-forming minerals. *Am. Miner.* **1983**, *68*, 277–279.
83. Bourdelle, F.; Cathelineau, M. Low-temperature chlorite geothermometry: A graphical representation based on a T–R²⁺–Si diagram. *Eur. J. Miner.* **2015**, *27*, 617–626. [[CrossRef](#)]
84. Hölttä, P.; Huhma, H.; Lahaye, Y.; Mänttari, I.; Lukkari, S.; O'Brien, H. Paleoproterozoic metamorphism in the northern Fennoscandian Shield: Age constraints revealed by monazite. *Int. Geol. Rev.* **2019**, *61*, 1–28. [[CrossRef](#)]
85. Evans, T.P. A method for calculating effective bulk composition modification due to crystal fractionation in garnet-bearing schist: Implications for isopleth thermobarometry. *J. Metamorph. Geol.* **2004**, *22*, 547–557. [[CrossRef](#)]
86. Kelsey, D.E.; Hand, M. On ultrahigh temperature crustal metamorphism: Phase equilibria, bulk compositions, heat sources, timescales and tectonic settings. *Geosci. Front.* **2015**, *6*, 311–356. [[CrossRef](#)]
87. Taylor, R.J.M.; Kirkland, C.L.; Clark, C. Accessories after the facts: Constraining the timing, duration and conditions of high-temperature metamorphic processes. *Lithos* **2016**, *264*, 239–257. [[CrossRef](#)]

88. Kohn, M.J.; Engi, M.; Lanari, P. Petrochronology: Methods and Applications. *Rev. Miner. Geochem.* **2017**, *83*, 1–575.
89. Kohn, M.J.; Corrie, S.L.; Markley, C. The fall and rise of metamorphic zircon. *Am. Mineral.* **2015**, *100*, 897–908. [[CrossRef](#)]
90. Rubatto, D. Zircon: The Metamorphic Mineral. *Rev. Mineral. Geochem.* **2017**, *83*, 261–295. [[CrossRef](#)]
91. Corfu, F.; Hanchar, J.M.; Hoskin, P.W.O.; Kinny, P. Atlas of zircon textures. *Rev. Mineral. Geochem.* **2003**, *53*, 469–500. [[CrossRef](#)]
92. Fornelli, A.; Langone, A.; Micheletti, F.; Piccareta, G. REE partition among zircon, orthopyroxene, amphibole and garnet in a high-grade metabasic system. *Geol. Mag.* **2018**, *155*, 1705–1726. [[CrossRef](#)]
93. Belousova, E.; Griffin, W.; O'Reilly, S.Y.; Fisher, N. Igneous zircon: Trace element composition as an indicator of source rock type. *Contrib. Miner. Pet.* **2002**, *143*, 602–622. [[CrossRef](#)]
94. Grimes, C.B.; Wooden, J.L.; Cheadle, M.J.; John, B.E. “Fingerprinting” tectono-magmatic provenance using trace elements in igneous zircon. *Contrib. Miner. Pet.* **2015**, *170*, 1–26. [[CrossRef](#)]
95. Engi, M. Petrochronology Based on REE-Minerals: Monazite, Allanite, Xenotime, Apatite. *Rev. Miner. Geochem.* **2017**, *83*, 365–418. [[CrossRef](#)]
96. Catlos, E.J.; Gilley, L.D.; Harrison, T.M. Interpretation of monazite ages obtained via in situ analysis. *Chem. Geol.* **2002**, *188*, 193–215. [[CrossRef](#)]
97. Kohn, M.J.; Malloy, M.A. Formation of monazite via prograde metamorphic reactions among common silicates: Implications for age determinations. *Geochim. Cosmochim. Acta* **2004**, *68*, 101–113. [[CrossRef](#)]
98. Wing, B.A.; Ferry, J.M.; Harrison, T.M. Prograde destruction and formation of monazite and allanite during contact and regional metamorphism of pelites: Petrology and geochronology. *Contrib. Miner. Pet.* **2003**, *145*, 228–250. [[CrossRef](#)]
99. Finger, F.; Broska, I.; Roberts, M.P.; Schermaier, A. Replacement of primary monazite by apatite-allanite-epidote coronas in an amphibolite facies granite gneiss from the eastern Alps. *Am. Mineral.* **1998**, *83*, 248–258. [[CrossRef](#)]
100. Townsend, K.J.; Miller, C.F.; D’Andrea, J.L.; Ayers, J.C.; Harrison, T.M.; Coath, C.D. Low temperature replacement of monazite in the Ireteba granite, Southern Nevada: Geochronological implications. *Chem. Geol.* **2001**, *172*, 95–112. [[CrossRef](#)]
101. Johnson, T.E.; Clark, C.; Taylor, R.J.M.; Santosh, M.; Collins, A.S. Prograde and retrograde growth of monazite in migmatites: An example from the Nagercoil Block, southern India. *Geosci. Front.* **2015**, *6*, 373–387. [[CrossRef](#)]
102. Seydoux-Guillaume, A.; Montel, J.; Bingen, B.; Bosse, V.; de Parseval, P.; Paquette, J.; Janots, E.; Wirth, R. Low-temperature alteration of monazite: Fluid mediated coupled dissolution–precipitation, irradiation damage, and disturbance of the U–Pb and Th–Pb chronometers. *Chem. Geol.* **2012**, *330–331*, 140–158. [[CrossRef](#)]
103. Budzyn, B.; Harlov, D.E.; Williams, M.L.; Jercinovic, M.J. Experimental determination of stability relations between monazite, fluorapatite, allanite, and REE-epidote as a function of pressure, temperature, and fluid composition. *Am. Mineral.* **2011**, *96*, 1547–1567. [[CrossRef](#)]
104. Sindors, S.; Gerdes, A.; Ronkin, Y.L.; Dziggel, A.; Hetzel, R.; Schulte, B.A. Monazite stability, composition and geochronology as tracers of Paleoproterozoic events at the eastern margin of the East European Craton (Taratash complex, Middle Urals). *Lithos* **2012**, *132*, 82–97. [[CrossRef](#)]
105. Harlov, D.E.; Harlov, D.E.; Wirth, R.; Wirth, R.; Hetherington, C.J.; Hetherington, C.J. Fluid-mediated partial alteration in monazite: The role of coupled dissolution–reprecipitation in element redistribution and mass transfer. *Contrib. Miner. Pet.* **2011**, *162*, 329–348. [[CrossRef](#)]
106. Hetherington, C.J.; Harlov, D.E.; Budzyń, B. Experimental metasomatism of monazite and xenotime: Mineral stability, REE mobility and fluid composition. *Mineral. Petrol.* **2010**, *99*, 165–184. [[CrossRef](#)]
107. Tropper, P.; Manning, C.E.; Harlov, D.E. Solubility of CePO₄ monazite and YPO₄ xenotime in H₂O and H₂O–NaCl at 800 °C and 1GPa: Implications for REE and Y transport during high-grade metamorphism. *Chem. Geol.* **2011**, *282*, 58–66. [[CrossRef](#)]
108. Williams, I.S. Response of detrital zircon and monazite, and their U–Pb isotopic systems, to regional metamorphism and host-rock partial melting, Cooma Complex, southeastern Australia. *Australian J. Earth Sci.* **2001**, *48*, 557–580. [[CrossRef](#)]

109. Rasmussen, B.; Muhling, J.R. Monazite begets monazite: Evidence for dissolution of detrital monazite and reprecipitation of syntectonic monazite during low-grade regional metamorphism. *Contrib. Miner. Pet.* **2007**, *154*, 675–689. [[CrossRef](#)]
110. Williams, M.L.; Jercinovic, M.J.; Harlov, D.E.; Budzyn, B.; Hetherington, C.J. Resetting monazite ages during fluid-related alteration. *Chem. Geol.* **2011**, *283*, 218–225. [[CrossRef](#)]
111. Pollington, A.D.; Baxter, E.F. High resolution Sm–Nd garnet geochronology reveals the uneven pace of tectonometamorphic processes. *Earth Planet. Sci. Lett.* **2010**, *293*, 63–71. [[CrossRef](#)]
112. Pollington, A.D.; Baxter, E.F. High precision microsampling and preparation of zoned garnet porphyroblasts for Sm–Nd geochronology. *Chem. Geol.* **2011**, *281*, 270–282. [[CrossRef](#)]
113. Baxter, E.F.; Scherer, E.E. Garnet Geochronology: Timekeeper of Tectonometamorphic Processes. *Elements* **2013**, *9*, 432–438. [[CrossRef](#)]
114. Baxter, E.F.; Caddick, M.J.; Dragovic, B. Garnet: A Rock-Forming Mineral Petrochronometer. *Rev. Mineral. Geochem.* **2017**, *83*, 469–533. [[CrossRef](#)]
115. Hölttä, P.; Huhma, H.; Mänttari, I.; Paavola, J. P–T–t development of Archaean granulites in Varpaisjärvi, Central Finland. *Lithos* **2000**, *50*, 121–136.
116. Käpyaho, A.; Hölttä, P.; Whitehouse, M.J. U–Pb zircon geochronology of selected Archaean migmatites in eastern Finland. *Bull. Geol. Soc. Finl.* **2007**, *79*, 95–115. [[CrossRef](#)]
117. Mikkola, P.; Huhma, H.; Heilimo, E.; Whitehouse, M. Archean crustal evolution of the Suomussalmi district as part of the Kianta Complex, Karelia; constraints from geochemistry and isotopes of granitoids. *Lithos* **2011**, *125*, 287–307. [[CrossRef](#)]
118. Mikkola, P.; Lauri, L.S.; Käpyaho, A. Neoproterozoic leucogranitoids of the Kianta Complex, Karelian Province, Finland; source characteristics and processes responsible for the observed heterogeneity. *Precambrian Res.* **2012**, *206–207*, 72–86.
119. Lauri, L.S.; Andersen, T.; Holttä, P.; Huhma, H.; Graham, S. Evolution of the Archaean Karelian Province in the Fennoscandian Shield in the light of U–Pb zircon ages and Sm–Nd and Lu–Hf isotope systematics. *J. Geol. Soc. Lond.* **2011**, *168*, 201–218. [[CrossRef](#)]
120. Lahtinen, R.; Sayab, M.; Karell, F. Near-orthogonal deformation successions in the polydeformed Paleoproterozoic Martimo belt: Implications for the tectonic evolution of Northern Fennoscandia. *Precambrian Res.* **2015**, *270*, 22–38. [[CrossRef](#)]
121. Tuisku, P.; Mikkola, P.; Huhma, H. Evolution of Migmatitic Granulite Complexes: Implications from Lapland Granulite Belt, Part I: Metamorphic geology. *Bull. Geol. Soc. Finl.* **2006**, *78*, 71–105. [[CrossRef](#)]
122. Tuisku, P.; Huhma, H. Evolution of Migmatitic Granulite Complexes: Implications from Lapland Granulite Belt, Part II: Isotopic dating. *Bull. Geol. Soc. Finl.* **2006**, *78*, 143–175. [[CrossRef](#)]
123. Evins, P.M.; Laajoki, K. Early Proterozoic nappe formation; an example from Sodankylä, Finland, northern Baltic Shield. *Geol. Mag.* **2002**, *139*, 73–87. [[CrossRef](#)]
124. Hölttä, P.; Väisänen, M.; Väänänen, J.; Manninen, T. Paleoproterozoic metamorphism and deformation in central Lapland, Finland. *Spec. Pap. Geol. Surv. Finl.* **2007**, *44*, 7–56.
125. Hanski, E. *Kallioperäkartta 1:100,000-Maps of Pre-Quaternary Rocks, Sheet 3614, Vikajärvi*; Geological Survey of Finland: Espoo, Finland, 2002.
126. Hölttä, P.; Heilimo, E. Metamorphic map of Finland. *Spec. Pap. Geol. Surv. Finl.* **2017**, *60*, 75–126.
127. Perchuk, L.L.; Krotov, A.V. Petrology of the mica schists of the Tanaelv Belt in the southern tectonic framing of the Lapland Granulite Complex. *Petrology* **1997**, *6*, 149–179.
128. Huhma, H. Isotope results from Lapland-Kola province in Finland. *GTK Open File Res. Rep.* **2019**, *37*, 44.

Publisher’s Note: MDPI stays neutral with regard to jurisdictional claims in published maps and institutional affiliations.



© 2020 by the authors. Licensee MDPI, Basel, Switzerland. This article is an open access article distributed under the terms and conditions of the Creative Commons Attribution (CC BY) license (<http://creativecommons.org/licenses/by/4.0/>).